

# Restoring Images Captured in Arbitrary Hybrid Adverse Weather Conditions in One Go

Ye-Cong Wan, Ming-Wen Shao *Member, IEEE*, Yuan-Shuo Cheng, Yue-Xian Liu, Zhi-Yuan Bao, and De-Yu Meng *Member, IEEE*,

**Abstract**—Adverse conditions typically suffer from stochastic hybrid weather degradations (e.g., rainy and hazy night), while existing image restoration algorithms envisage that weather degradations occur independently, thus may fail to handle real-world complicated scenarios. Besides, supervised training is not feasible due to the lack of comprehensive paired dataset to characterize hybrid conditions. To this end, we have advanced the forementioned limitations with two tactics: framework and data. On the one hand, we present a novel unified framework, dubbed RAHC, to Restore Arbitrary Hybrid adverse weather Conditions in one go, which can comfortably cope with hybrid scenarios with insufficient remaining background constituents and restore arbitrary hybrid conditions with a single trained model flexibly. On the other hand, we establish a new dataset, termed HAC, for learning and benchmarking arbitrary Hybrid Adverse Conditions restoration. HAC contains 31 scenarios composed of an arbitrary combination of five common weather, with a total of  $\sim 316K$  adverse-weather/clean pairs. As for fabrication, the training set is automatically generated by a dedicated AdverseGAN with no-frills labor, while the test set is manually modulated by experts for authoritative evaluation. Extensive experiments yield superior results and in particular establish new state-of-the-art results on both HAC and conventional datasets.

**Index Terms**—Hybrid weather conditions, Unified framework, Data generation.

## 1 INTRODUCTION

IN real-world adverse scenarios, different weather degradations often occur simultaneously in an uncertain way, e.g., snowy night, rainy night. Images captured under these conditions inevitably incur abysmal visibility and corrupted feature remnants, and the stochastic hybrid disruption may dramatically hamper outdoor high-level vision systems such as autonomous driving systems [1], [2], [3] and surveillance systems [4]. Unfortunately, prominent algorithms [5], [6], [7], [8] deal with each weather degradation individually ignoring the hybrid degradation characterization of combined action. Specifically, early researchers focused on developing task-specific restoration algorithms for given weather conditions [9], [10], [11], [12], [13], [14] (Fig. 1(a)). Afterwards various generic networks were proposed to handle different degradations with identical architecture [15], [16], [17], [18], [19] (Fig. 1(b)), but with different weights for different tasks. To address this issue, recent researches aim at restoring degradation under multiple adverse conditions with a single unified model [20], [21], [22], [23], [24] (Fig. 1(c)). While combined rain and haze scenes were evaluated [21], [23], [24], more hybrid conditions and more complex hybrid combinations remain untapped by these methods especially when there are more than two weather degradations mixed together. Despite few task-specific works [25], [26], [27] have partly explored restoring two-weather superimposed scenarios, they were designed for specialized combinations (e.g., rain streak and raindrop) and unable to

be extended to other real-world diverse hybrid scenarios.

To more flexibly and practically deal with real-world scenarios, a turnkey solution that can restore arbitrary hybrid adverse conditions in one go is imminent. Compared to this goal, the existing works have the following limitations. In terms of framework, (i) existing restoration networks are limited in characterizing hybrid multiple weather degradations simultaneously due to the lack of a multi-subspace feature extraction mechanism. (ii) Models utilized in single degradation removal are restricted in restoring hybrid adverse weather conditions with insufficient remaining background constituents. (iii) Previous unified learning strategies are designed for non-overlapping degradations and are constrained to popularize to diverse hybrid scenarios. In terms of data, (i) existing datasets only cover separate single or special double weather degradations without various hybrid conditions. (ii) Collecting real-world paired data would be virtually infeasible, due to uncontrollable factors, e.g., wind, lighting, and camera shifts. (iii) Manual synthesis of massive paired data with hybrid adverse weather conditions tends to be time-consuming and labor-consuming.

With the above observations, there are two posers need to answer: (1) How to construct a unified framework that can flexibly tackle real-world diverse hybrid scenarios with a single trained model? (2) How to effectively establish a comprehensive paired dataset that includes an exhaustive list of all possible real-world adverse weather conditions?

To tackle the aforementioned problems, in this paper, we propose a novel unified framework RAHC and a new hybrid dataset HAC to restore arbitrary hybrid adverse weather conditions in one go (Fig. 1(d)). For the framework RAHC, there are three innovations for defeating the above limitations. (1) Multi-Head Blend Block (MHBB) for multi-weather degradation representation: the multi-head mech-

- Y.-C. Wan, M.-W. Shao, Y.-S. Cheng, Y.-X. Liu, and Z.-Y. Bao are with the College of Computer Science and Technology, China University of Petroleum, China.
- D.-Y. Meng is with the Institute for Information and System Sciences, Xi'an Jiaotong University, China.

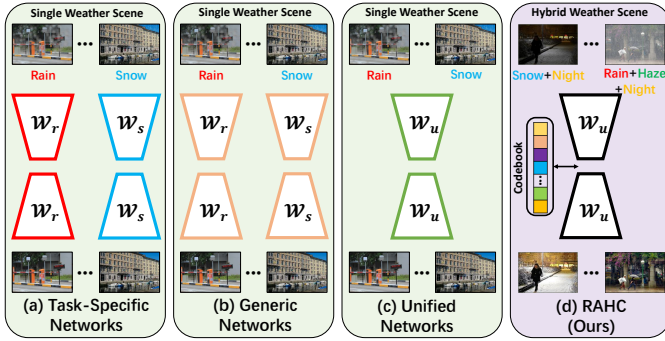


Fig. 1. Overview of adverse conditions restoration frameworks. (a) Separate networks designed for specific tasks; (b) generic networks with task-specific weights; (c) unified all-in-one networks with single trained weights; (d) our proposed RAHC framework. In contrast to existing approaches that aim to tackle conditions with a single weather type, RAHC can handle arbitrary hybrid adverse weather conditions in one go, thus enjoying better flexibility and practicality in realistic applications.

anism overriding the blend operator of convolution and attention can provide multiple “representation subspaces” [28] as well as complementary feature for multi-weather learning. (2) Reconstruction vectors aided restoration for hybrid conditions with limited image constituents retention: we propose using discrete representations from the Codebook [29] pre-trained on large-scale natural images to. These discrete representations, which we refer to as reconstruction vectors, can provide additional visual content cues to auxiliary the reconstruction of realistic and clean output. (3) Output space discrimination for efficient arbitrary hybrid conditions restoration: we design a simple multilabel-classification discriminator from the output space to encourage the restoration network to learn degradation-agnostic repair capabilities, which enable RAHC to flexibly handle diverse hybrid scenarios without requiring complex strategies or modules. Notably, this protocol can be seamlessly integrated into existing universal image restoration algorithms in a non-destructive manner, enhancing their performance in the all-in-one multi-weather removal setting.

For the construction of hybrid adverse weather conditions dataset HAC, there are  $\sim 316K$  pairs of  $2^5 - 1 = 31$  adverse conditions with five common weather types (namely haze, rain streak, snow, night, and raindrop) arranged in combination except for the clean one. To synthesize sufficient and diverse pairwise data efficiently and at low consumption, we develop a powerful generator AdverseGAN to learn from adverse conditions so as to approximate the degradation implicitly rather than expensive manual labeling. Thus, the training set can be automatically generated by AdverseGAN with minimal labor cost. On the contrary, the test set is meticulously handcrafted by our recruited experts for authoritative evaluation. The domain gap between the training and test sets allows for better evaluation of the generalization ability which is critical for real-world applications, especially when the real data is infeasible. Comprehensive experimental results substantiate the superiority of the RAHC beyond state-of-the-art restoration methods on both HAC and conventional datasets.

In conclusion, the main contributions are summarized as follows:

- We propose a novel framework, dubbed RAHC, to restore diverse hybrid adverse weather conditions while enjoying the properties of being concise, flexible, and powerful.
- We present a multi-head blend block to provide multiple representation subspaces for multi-degeneration learning. Meanwhile, a reconstruction vectors aided restoration scheme is devised for severely deteriorated hybrid adverse conditions, as well as an output space discrimination regime for unified learning of diverse hybrid degradations.
- A new synthetic dataset HAC for arbitrary hybrid adverse weather conditions restoration is constructed. To the best of our knowledge, HAC is the first to encompass such a wide range of scenarios and provides the most comprehensive benchmark for this task.
- Solid and promising experimental results on HAC and conventional datasets demonstrate the effectiveness, superiority, and robustness of our proposed RAHC.

## 2 RELATED WORK

### 2.1 Adverse Weather Conditions Restoration

Numerous algorithms have been proposed to recover images captured in adverse weather conditions, e.g., rain [12], [30], haze [31], [32], [33], snow [9], [34], etc. While these methods perform well on the specific weather type, significant performance degradation was observed when migrating to other tasks. Aiming at this limitation, a broad spectrum of research [15], [16], [17], [35], [36] has explored generic frameworks to accommodate different degradation types with an identical network. Even so, they still require separate training of independent weights for each task, hindering its generalizability. To repair multiple degradations in an all-in-one fashion, several unified models are proposed [20], [21], [22], [23], [24]. However, these approaches ignore that real-world adverse conditions often suffer from superimposed multiple degradations [25], e.g., rain streaks and raindrops [26], rain and nighttime [27], etc. Although several methods [21], [23], [24] include the superposition of two weather (rain and fog) at test time, they suffer from relatively limited image constituents retention as well as inadequate multi-degradation characterization mechanism when there are more than two degradations in the hybrid condition. Meanwhile, the unified learning strategies of these methods are constrained in modeling hybrid multiple degradations simultaneously. On the contrary, in this paper, adverse scenarios with an arbitrary hybrid of five weather types are considered for a total of 31 conditions, and RAHC can cope with all conditions in one go driving arbitrary hybrid adverse conditions restoration in a broad sense.

### 2.2 Pseudo Data Generation

Data-driven vision tasks rely heavily on high-quality datasets. Unfortunately, the labeling and acquiring of data tends to be expensive, challenging and time-consuming. To surmount this bottleneck, several recent efforts [37], [38], [39], [40] delve into pseudo-data generation by leveraging Generative Adversarial Networks (GAN). For instance, Zhang *et al.* [37] proposed a DatasetGAN to synthesize

highly realistic images with pixel-wise annotations, the model trained on the synthetic dataset can even surpass the ones trained on the real dataset. Yang *et al.* [38] released SurfGAN, which facilitates the training of autonomous driving models by simulating realistic road scenarios. In addition to high-level tasks, this research boom has also been conveyed to low-level tasks. Wang *et al.* [39] exceeded SOTA with only 0.17% original data and synthesized pseudo-data. Yue *et al.* [41] introduced a dual adversarial network to simultaneously tackle noise removal and noise generation. Inspired by CycleGAN [42], Wei *et al.* [43] generated a pseudo-paired dataset Rain200A by cycle translation, and the models trained on it exhibit better robustness and generalization. Inspired by these pioneer works, we pursue the efficient and inexpensive synthesis of paired data for training by utilizing a deliberate GAN.

### 2.3 Perceptual Image Compression

Tremendous success in two-stage image generation [29], [44], [45], [46], [47] based on perceptual image compression has been witnessed. These works compress images into discrete latent vectors in the first stage and synthesize high-quality images leveraging encoded vectors in the second stage. In this paper, we focus on perceptual image compression in the first stage. VQVAE [46] first presents an auto-encoder model to implement multi-scale quantization of images. Based on VQVAE, VQGAN [29] introduces adversarial and perceptual objectives to obtain higher compression rates while preserving satisfactory perceptual quality. Furthermore, LDM [47] explores different compression rates and different kinds of regularizations, deriving a compression model that is more adept at preserving details. Intrigued by the extensive image priors contained in the discrete latent vectors of image compression, we advocate utilizing these auxiliary priors to guide the restoration, since the discrete vectors comprise context-rich visual parts.

### 2.4 Unsupervised Domain Adaptation (UDA)

UDA algorithms [48], [49], [50], [51], [52], [53], [54] for semantic segmentation aim to constrain the model trained on the source domain to learn domain-invariant features, thereby generalizing to the target domain. One category of these studies [51], [52], [53], [54] was devoted to training a discriminator to distinguish whether the output results come from the source or target domain, while the segmentation network learns domain-invariant knowledge to confuse the discriminator. Motivated by these methods, RAHC interestingly treats the unified restoration of different degradations as a domain adaptive problem, i.e., no matter which degradation the image suffers, the restored result should be a degeneration-agnostic high-quality clean image. As will be demonstrated, fooling a degradation-type classifier is more straightforward and concise than sophisticated units and training strategies in degradation-agnostic feature learning.

## 3 METHODOLOGY

We first present an overview of our proposed tactics for arbitrary hybrid adverse weather conditions restoration in Sec 3.1. Then we introduce the restoration network as well

as the core elements in Sec 3.2, and describe the output space discriminative learning scheme in Sec 3.3. Finally, we discuss and detail our adverse conditions generator AdverseGAN in Sec 3.4.1 and the established HAC dataset in Sec. 3.4.2.

### 3.1 Overview of the Proposed Method

The training procedure for RAHC is illustrated in Fig. 2. RAHC aims to tackle arbitrary hybrid adverse conditions restoration via a unified framework, and the central notion is to generate adequate paired data using AdverseGAN with minimal labor costs, and training a degradation-agnostic restoration network through a discriminative learning scheme. Simultaneously, the framework also incorporates visual constituents embedded in the Codebook to provide auxiliary cues for restoring highly challenging hybrid conditions. Formally, given an adverse condition  $D \in \mathbb{R}^{H \times W \times 3}$  generated by AdverseGAN and corresponding clean counterpart  $C \in \mathbb{R}^{H \times W \times 3}$ , the degraded image  $D$  is first fed into the restoration network to produce the restored clean image  $R \in \mathbb{R}^{H \times W \times 3}$ . Meanwhile, the feature mapping network learns the projection from the encoded feature to corresponding clean embedding to locate the reconstruction vectors in the Codebook, supplying additional auxiliary visual atoms for restoration. Finally, the restored result is input into the discriminator to distinguish the type of degradation, while the restoration network tries to restore degradation-agnostic image to confuse the discriminator. The whole procedure is a snap, and there is no extra inference cost or modification during testing besides the restoration network.

### 3.2 Network Architecture

The restoration network adheres to a U-shaped structure, which hierarchically cascades multiple tailored multi-head blend blocks, and the knowledge domain is broadened at the bottleneck supported by reconstruction vectors, thereby leading to more optimal repair results. Mathematically, given a degraded image  $D \in \mathbb{R}^{H \times W \times 3}$ , a  $3 \times 3$  convolution is first adopted to produce shallow feature embeddings  $F_{in} \in \mathbb{R}^{H \times W \times C}$ . Then,  $F_{in}$  is propagated through four encoder layers built upon MHBB to obtain the deep feature  $F_{mi} \in \mathbb{R}^{\frac{H}{8} \times \frac{W}{8} \times 8C}$ . Thereafter,  $F_{mi}$  is transmitted by the feature mapping network to locate the reconstruction vectors  $F_{rv} \in \mathbb{R}^{\frac{H}{8} \times \frac{W}{8} \times N_z}$  that most likely can reconstruct the hidden clean image from the Codebook, where  $N_z$  represents the dimension of reconstruction vector. Eventually,  $F_{mi}$  and  $F_{rv}$  are concatenated together and fed into the symmetric decoder to recover the final result  $R \in \mathbb{R}^{H \times W \times 3}$  via a  $3 \times 3$  convolution. Next, we will describe the core components of the proposed restoration network.

*Multi-Head Blend Block (MHBB)*. Existing feature extraction modules lack a multi-degradation representation mechanism to capture the characteristics of hybrid multiple weather, leading to inadequate feature modeling. Besides, the complementary properties of convolution, which has strong local computational capabilities, and Transformer, which is excellent at capturing long-range dependencies, make the hybrid structure a better alternative for feature extraction [55], [56]. To this end, we propose a Multi-Head

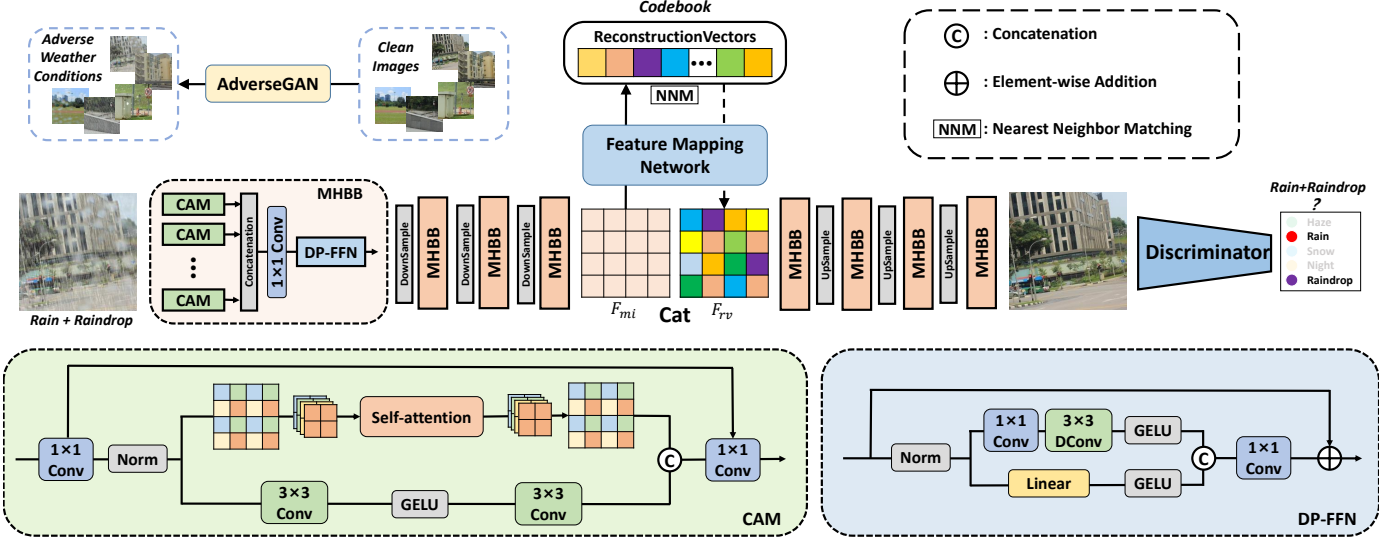


Fig. 2. Illustration of the proposed RAHC architecture. The restoration network consists of an encoder, a decoder, and a feature mapping network. The encoder and decoder are both cascaded from multiple MHBBs. The mapping network first maps the encoded feature to the latent clean space and then locates the reconstruction vectors in the pre-established Codebook by nearest neighbor matching to provide privileged visual cues for the decoder. To enable degradation-agnostic learning, we utilize a discriminator to distinguish the type of the weather degradation from the restored image while the restoration network struggles to fool the discriminator. Schematic diagrams for Multi-Head Blend Block (MHBB), Convolution-Attention Module (CAM), and Dual-Path Feed-Forward Network (DP-FFN) are illustrated in colored dashed boxes.

Blend Block (MHBB) to provide multiple “representation subspaces” as well as complementary features for multi-weather learning. Fig. 2 illustrates the two core units (CAM & DP-FFN) of MHBB. Rather than simply combining Transformer and Convolution in parallel or series, we treat convolution and self-attention as equivalent micro-level operators and deploy them in parallel. By applying a multi-head mechanism that overrides the blend parallel operator, the proposed block is able to provide multi-degradation representation subspaces for unified learning. More concretely, an input feature  $X$ , is first divided into “heads” which bears a resemblance to the vanilla Transformer [28]. The multi-head design allows separate branches to learn different representations and thus adaptively extract different degradation cues to guarantee the ability of diversity restoration. Then, each head is transformed by a CAM. CAM contains two branches: the attention path and the convolution path, which are split and merged for parallel processing with the addition of  $1 \times 1$  convolution. To reduce the high computational effort of vanilla self-attention while preserving the global computational properties, we adopt the pixel-shuffle [57] operator in the attention path to diminish the number of tokens while avoiding information loss. The convolution path, on the other hand, consists of two convolutional layers and a GELU activation function. We formulate such a process as:

$$\begin{aligned}
 X_k^a, X_k^b &= \text{Split}(\text{Norm}(\text{Conv}_{1 \times 1}(X_k))), \\
 \hat{X}_k^a &= \text{PS}(\text{Self-Attention}(\text{PU}(X_k^a))), \\
 \hat{X}_k^b &= \text{Conv}_{3 \times 3}(\text{GELU}(\text{Conv}_{3 \times 3}(X_k^b))), \\
 \hat{X}_k &= \text{Conv}_{1 \times 1}(\text{Cat}(\hat{X}_k^a, \hat{X}_k^b)) + X_k,
 \end{aligned} \tag{1}$$

where  $k$  represents the  $k_{th}$  head,  $PU$  and  $PS$  denote pixel-unshuffle and pixel-shuffle operations. Subsequently, the results of different heads are integrated together with a stacked  $1 \times 1$  convolutional.

Locally relevant information is crucial for image restoration, while the original Feed-Forward Network (FFN) is insensitive and inept at this demand since it processes each token independently without considering the relationships between them. Considering that the convolution operation can capture local contextual information by sharing weights over neighboring pixels. To compensate for the above limitations, we present a Dual-Path FFN (DP-FFN) to extract local contextual information by introducing convolutional branches parallel with a fully connected layer. The process of DP-FFN is formulated as:

$$\begin{aligned}
 \hat{Y}_1, \hat{Y}_2 &= \text{Split}(\text{Norm}(\hat{Y})), \\
 Y_1 &= \text{GELU}(\text{Linear}(\hat{Y}_1)), \\
 Y_2 &= \text{GELU}(\text{DConv}_{3 \times 3}(\text{Conv}_{1 \times 1}(\hat{Y}_2))), \\
 Y &= \text{Conv}_{1 \times 1}(\text{Cat}(Y_1, Y_2)) + \hat{Y},
 \end{aligned} \tag{2}$$

where  $\text{DConv}_{3 \times 3}$  represents  $3 \times 3$  depthwise convolution with group number equal to channel dimension.

Overall, the MHBB process can be expressed as:

$$\begin{aligned}
 \hat{Y} &= \text{Cat}(\text{CAM}_1(X_1), \text{CAM}_2(X_2), \dots, \text{CAM}_k(X_k)), \\
 Y &= \text{DP-FFN}(\text{Conv}_{1 \times 1}(\hat{Y})).
 \end{aligned} \tag{3}$$

*Reconstruction Vectors Aided Restoration.* Existing image restoration algorithms intend to recover the degraded image from the remaining ambiguous background content. In this case, the available features are limited, especially hybrid conditions, and it is extremely challenging to recover high-quality images with insufficient information. Inspired by two-stage image generation models, which build a Codebook with rich context in the first stage and then generate images with encoded discrete vectors in the second stage. We utilize the context-rich vectors embedded in the Codebook to assist the network in repairing hybrid degraded images, which allows the knowledge domain of restoration to be extended from a single image to the entire vectors

repository. Benefiting from the information-rich image components contained in the reconstruction vectors, the restoration network can better reconstruct high-quality images.

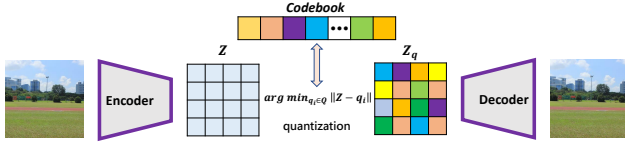


Fig. 3. Brief illustration of VQGAN model [29].

We first briefly describe the VQGAN model, which is proposed by Esser *et al.* [29] for two-stage image generation. VQGAN consists of an encoder E, a codebook Q with discrete codes, and a decoder G. Given an input image  $x \in \mathbb{R}^{H \times W \times 3}$ , the encoder E first embeds  $x$  to latent representation  $Z \in \mathbb{R}^{\frac{H}{f} \times \frac{W}{f} \times N_z}$ , where  $f$  and  $N_z$  are downsampling factor and the dimension of latent vectors, respectively. Then, a quantization  $q(\cdot)$  is performed on each representation vector  $z \in \mathbb{R}^{N_z}$  to locate the most similar discrete vector  $q_i$  in the Codebook.

$$Z_q = q(Z) := (\arg \min_{q_i \in Q} \|z - q_i\|) \in \mathbb{R}^{\frac{H}{f} \times \frac{W}{f} \times N_z}. \quad (4)$$

Finally, the decoder G reconstructs the output image  $\hat{x}$  from the quantized representation  $Z_q$ . The whole process of encoding, quantizing, and reconstructing can be expressed as follows:

$$\hat{x} = G(Z_q) = G(q(E(x))). \quad (5)$$

With the knowledge about VQGAN, the innovation of this paper can be better understood. To be specific, we utilize the VQGAN [29] pre-trained on OpenImages [58] with 8192 quantization encodings as a library of reconstruction vectors. The schematic illustration of this scheme is depicted in Fig. 4. The VQGAN encoder first produces the quantized encoding  $F_{rv}^c \in \mathbb{R}^{\frac{H}{8} \times \frac{W}{8} \times N_z}$  of the clean image, and for the degraded image feature  $F_{mi}$  encoded by the restoration network encoder, the mapping network learns to predict the possible embedding  $F_{rv}^d$  that consistent with  $F_{rv}^c$ . Attention and convolution layers are cascaded to construct the mapping network which can be optimized by the following cosine similarity loss.

$$\mathcal{L}_{map} = \sum_{i=0}^{\frac{W}{8}} \sum_{j=0}^{\frac{H}{8}} \left[ 1 - \frac{\cos(F_{rv}^d(i, j), F_{rv}^c(i, j))}{\frac{W}{8} \times \frac{H}{8}} \right]. \quad (6)$$

We can then obtain  $F_{rv}$  by leveraging a subsequent nearest neighbor matching  $NNM(\cdot)$  of each spatial encoding  $F_{rv}^d(i, j) \in \mathbb{R}^{N_z}$  from  $F_{rv}^c \in \mathbb{R}^{\frac{H}{8} \times \frac{W}{8} \times N_z}$  onto its closest reconstruction vector  $rv_k$  in the Codebook.

RAHC approximates quantized reconstruction vectors by mapping networks rather than predicting logits directly. The advantages are mainly twofold: (1) the transform dimension of the feature mapping is equal to the length of the quantized vector 256, while the dimension of the direct prediction is the size of the whole Codebook 8192, thus our mapping network is more lightweight. (2) Compared with direct classification to predict the reconstruction vectors, feature mapping followed by quantization would be less challenging and yield more accurate results (see Sec. 4.5.3).

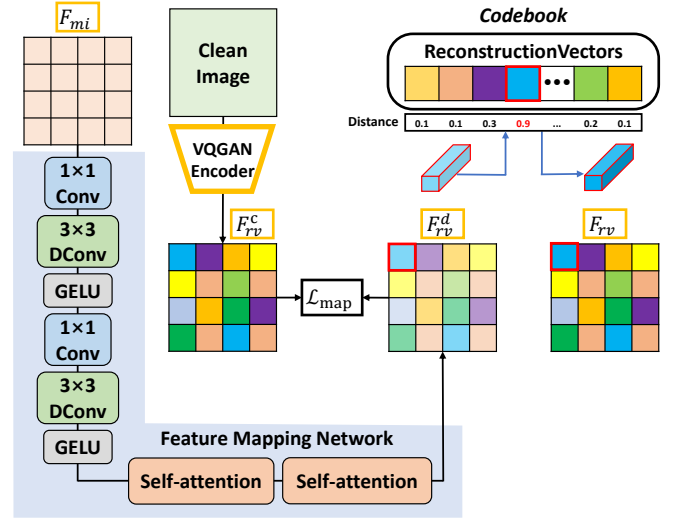


Fig. 4. Detailed illustration of reconstruction vectors aided scheme.

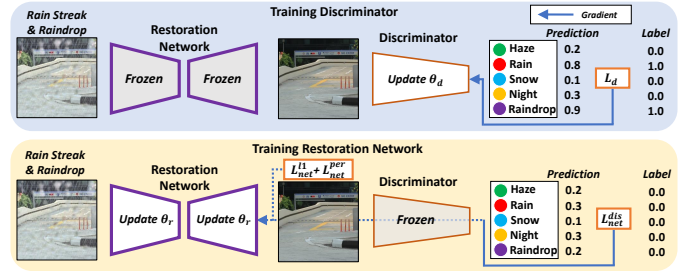


Fig. 5. Detailed illustration of output space discriminative learning scheme.

### 3.3 Output Space Discrimination for Efficient Arbitrary Hybrid Conditions Restoration

Existing all-in-one restoration approaches rely on distillation [20], degradation guidance [22], and querying [23] to gain knowledge of different degradations. Although these methods achieve excellent performance for non-overlapping degradation, they are limited in modeling the joint characterization of hybrid multiple degradations. Our intuition is that regardless of the degradation type image suffered, the restored result should be a degeneration-agnostic high-quality clean image. Thus, we innovatively treat the unified learning of multiple degradations as a domain adaptive problem and cultivate the degradation-agnostic adaptive restoration network via discriminative adversarial learning scheme. In contrast to Li *et al.* [21] that strives to reserve degradation cues to train multiple feature extractors, we dedicate to back-constraining the restoration network to yield consistent degradation-agnostic ideal images.

Based on the concept of adversarial gaming, the discriminator aims to identify from the restored image which degradations it suffered. On the contrary, the restoration network endeavors to yield consistent untracked images to confuse the discriminator. The detailed engraving is given in Fig. 5.

*Discriminator Training.* Given the restoration output  $R = Network(D)$ , we forward  $R$  to discriminator  $Dis$  to distinguish the type of weather degradation from the restored image. The training of the discriminator can be regarded as

a multilabel classification task, and the cross-entropy loss objective can be defined as:

$$\mathcal{L}_d = \sum_{i=0}^{n-1} [-t_i \log \text{Dis}(R)_i - (1 - t_i) \log(1 - \text{Dis}(R)_i)], \quad (7)$$

where  $n$  denotes the number of degenerate types,  $t_i = 1$  if  $I$  suffer from degradation  $i$  else  $t_i = 0$ .

*Restoration Network Training.* First, pixel-level L1 loss is equipped to allow the restoration results  $R$  to approximate the ground truth clean image  $C$ :

$$\mathcal{L}_{net}^{l1} = \|R - C\|_1. \quad (8)$$

Second, to allow restoring degeneration-agnostic results, i.e., results that can not be recognized by the discriminator what degeneration types suffered, a discriminative loss is employed:

$$\mathcal{L}_{net}^{dis} = \sum_{i=0}^n -\log(1 - \text{Dis}(R)_i). \quad (9)$$

The ultimate goal is to minimize the L1 loss while allowing the results to approximate consistent degradation-agnostic clean distribution. Meanwhile, perceptual loss  $\mathcal{L}_{net}^{per}$  [59] is also employed to weaken the interference of noise from pseudo-data on the training. Thus, the final training objective can be expressed as:

$$\mathcal{L}_{net} = \mathcal{L}_{net}^{l1} + \lambda_{dis} \mathcal{L}_{net}^{dis} + \mathcal{L}_{net}^{per}, \quad (10)$$

where  $\lambda_{dis}$  is set to 0.1 to balance relative weight of  $\mathcal{L}_{net}^{dis}$ .

The proposed paradigm can cope with 31 hybrid weather conditions by relying only on a five-class classification discriminator, whereas existing approaches have to treat 31 scenarios separately and are limited in capturing cross-weather interrelationships.

### 3.4 Hybrid Adverse Conditions Dataset (HAC)

#### 3.4.1 AdverseGAN for Training Set Generation.

Pseudo-data generation [37], [38], [39], [40], [41], [43], [60] has been shown to be feasible and has achieved notable performance. Inspired by the above research, to save time and effort in building dataset for end-to-end training of arbitrary hybrid adverse conditions restoration, we propose to generate pseudo-adverse conditions with GAN rather than artificial processing. The key insight is to firstly train an elaborated AdverseGAN that can generate five non-hybrid weather conditions and then hybrid conditions can be generated by recursive calls. Therefore, ultimately we can automatically generate 31 adverse conditions automatically without manual operation. Schematic illustration of the AdverseGAN is provided in Fig. 6.

*Generator.* Following recent works [61], [62], [63], [64], our generator is constructed based on a dual space structure, content space  $\mathcal{C}$  and style space  $\mathcal{S}$ . The generator first encodes the input clean image into latent space and then generates the degraded image with the injection of style vector  $z_s$  and content vector  $z_c$  randomly drawn from a normal distribution. Type vector  $z_t$  mapping from type label  $t$  is integrated together to control condition type like cGAN [65]. The injection of style vector and content vector follow StyleGAN2 [66] and SNI [63] respectively. Conversely, the functions of our content latent space are different from SNI

which can be summarized in the following three aspects: (1) content code and image code are concatenated together as input feature map of the decoder achieving natural decoupling of clean background and degradation; (2) a separate content space separate from the style space can generate richer and more diverse conditions; (3) dual space allows for better disentanglement of content and style to generate more realistic and reliable adverse conditions.

After introducing dual space, the generation procedure from clean image  $C$  to corresponding degraded image  $D^t$  can be depicted by the conditional distribution  $p(D^t|C, t, z_c, z_s)$ . The generator  $G$  expresses an implicit distribution  $p_G(D|C, t, z_c, z_s)$  to approximate the true distribution  $p(D^t|C, t, z_c, z_s)$ . The pseudo degraded image  $D$  can be easily obtained:

$$z_c \sim p(z_c), z_s \sim p(z_s), D = G(C, t, z_c, z_s), \quad (11)$$

where  $p(i)$  denotes the distribution of the latent variable  $i$ . *Discriminators.* Although paired datasets of individual degradation types are readily available, most of them are synthetic data by artificial modulation and are unable to simulate real degradation scenarios well. In addition, generative adversarial networks cannot guarantee that the background of the generated images remains constant except for degradation. In order to remedy the above limitations, dual discriminators were introduced to generate more realistic and content-preserved adverse conditions. Realism-discriminator (*RD*) tries to distinguish between real-world adverse weather conditions and generated fake weather conditions. And pairing-discriminator (*PD*) tries to distinguish between real pairing data and pseudo pairing data, i.e., constraining the background consistency of the generated images. To allow multiple adverse conditions generation, our discriminator produces probability distributions over both sources and condition types [67],  $D: \mu \rightarrow Dsrc(\mu), Dcls(\mu)$ .

For *RD*, the adversarial loss is first deployed to constrain the generated image  $D$  to be indistinguishable from the real-world image  $E$ . The loss can be written as:

$$\mathcal{L}_{adv}^{RD} = \mathbb{E}_r[\log RDsrc(E)] + \mathbb{E}_{C,t,z_c,z_s}[\log(1 - RDsrc(G(C, t, z_c, z_s)))] \quad (12)$$

Apart from adversarial loss, type classification loss is also imposed to guarantee that the generated weather type meets expectations. We decompose the loss into two terms: a type classification loss of real-world images used to optimize *RD*, and a type classification loss of generated images used to optimize *G*. In detail, the former is defined as:

$$\mathcal{L}_{cls(r)}^{RD} = \mathbb{E}_{E,\hat{t}}[-\log RDcls(\hat{t}|E)]. \quad (13)$$

where  $\hat{t}$  represents the predicted weather type. On the other hand, the latter can be defined as:

$$\mathcal{L}_{cls(f)}^{RD} = \mathbb{E}_{C,t,z_c,z_s}[-\log RDcls(t|G(C, t, z_c, z_s))]. \quad (14)$$

Likewise, *PD* also contains two loss objectives, the adversarial loss for constraining the pairing of generated images and clean counterparts and the type classification loss for ensuring the pairing type matched expectation. The adversarial loss for optimizing *PD* can be expressed as:

$$\mathcal{L}_{adv}^{PD} = \mathbb{E}_{C,H}[\log PDsrc(C, H)] + \mathbb{E}_{C,t,z_c,z_s}[\log(1 - PDsrc(C, G(C, t, z_c, z_s)))] \quad (15)$$

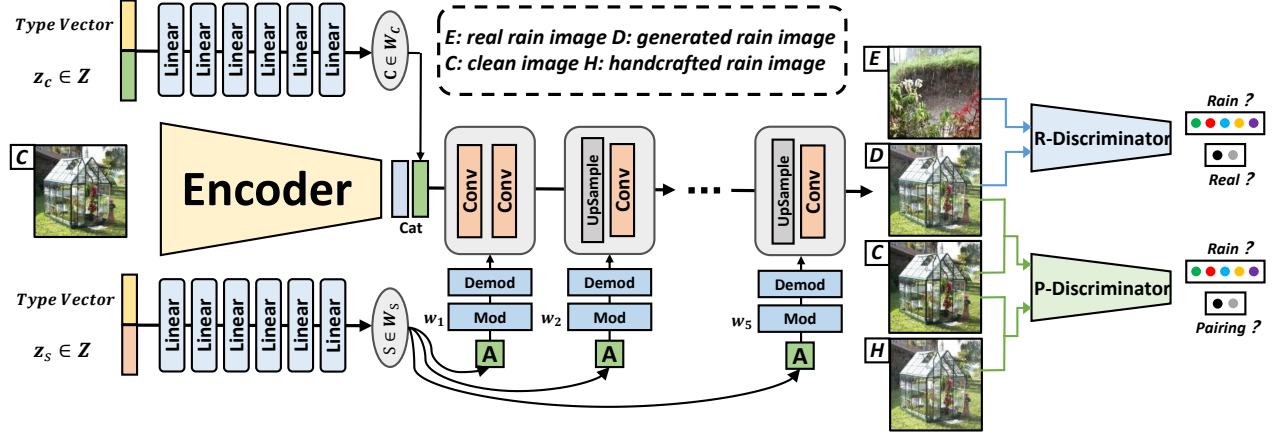


Fig. 6. Pipeline of our proposed AdverseGAN. The generator is an encoder-decoder structure, consisting of two latent space injection branches: content branch (top) and style branch (bottom). And there are two discriminators: Realism-Discriminator (R-Discriminator) and Pairing-Discriminator (P-Discriminator). R-Discriminator is designed to constrain the realism of the weather degradation, while P-Discriminator guarantees the matching with the input, i.e., the background is consistent, and only the weather is added. For brevity, we take the generation of rain streaks as an example, the other four weather types are similar. It is worth noting that AdverseGAN can generate different adverse conditions by controlling type vector and without have to train five separate models.

Correspondingly, the type classification loss utilized to optimize  $PD$  and  $G$ , respectively, are represented as:

$$\mathcal{L}_{cls(r)}^{PD} = \mathbb{E}_{C,H,t}[-\log PDcls(\hat{t}|C,H)], \quad (16)$$

$$\mathcal{L}_{cls(f)}^{PD} = \mathbb{E}_{C,t,z_c,z_s}[-\log PDcls(t|C,G(C,t,z_c,z_s))]. \quad (17)$$

*Full Objective.* Finally, the objective functions to optimize  $G$ ,  $RD$ , and  $PD$  are written, respectively, as

$$\mathcal{L}_G = \alpha(-\mathcal{L}_{adv}^{RD} + \lambda_{cls}\mathcal{L}_{cls(f)}^{RD}) + \beta(-\mathcal{L}_{adv}^{PD} + \lambda_{cls}\mathcal{L}_{cls(f)}^{PD}), \quad (18)$$

$$\mathcal{L}_{RD} = \alpha(\mathcal{L}_{adv}^{RD} + \lambda_{cls}\mathcal{L}_{cls(r)}^{RD}), \quad (19)$$

$$\mathcal{L}_{PD} = \beta(\mathcal{L}_{adv}^{PD} + \lambda_{cls}\mathcal{L}_{cls(r)}^{PD}), \quad (20)$$

where  $\alpha$ ,  $\beta$ , and  $\lambda_{cls}$  are hyper-parameters that balance the weights of each term and are set to 1, 2 and 3, respectively. To unify the learning rate and avoid mode collapse, both  $\mathcal{L}_{RD}$  and  $\mathcal{L}_{PD}$  are modulated by  $\alpha$  and  $\beta$ . Thanks to the decoupled design and pairing-discriminator which has served as a content preserver, cycle consistency loss is not introduced since it is time-consuming and resource-intensive.

In this paper, we have considered  $2^5 - 1 = 31$  combinations for arbitrary hybrid adverse conditions restoration (five weather types arranged in combination except for the clean one). To cost-effectively synthesize sufficient paired data for end-to-end training, the enormous amount of training data is produced by AdverseGAN almost without any labor cost. We first train the AdverseGAN which can generate five basic adverse weather conditions by leveraging existing data, and then superimposed hybrid scenarios can be generated by recursive calls. Ultimately, the production of the training set can be done automatically by AdverseGAN. The datasets for training AdverseGAN are summarized in Tab. 1.

After training, we manually curate 5000 well-illuminated outdoor clean images from three datasets [10], [34], [68] as the groundtruth. Then each image is randomly cropped to a fixed size of  $256 \times 256$ . Thereafter, for each cropped image,

TABLE 1

Summary of the dataset for AdverseGAN training. It is worth noting that all data are from the training set and 10% of real-world images were split out for the visual testing purpose.

Adverse Condition	Paired Data	Real-world Data
Haze	OTS [68]	Li <i>et al.</i> [68]
Rain Streak	Rain12000 [7]	Wei <i>et al.</i> [69]
Snow	Snow100K [34]	Liu <i>et al.</i> [34]
Night	SICE [70]	Loh <i>et al.</i> [71]
Raindrop	Raindrop [10]	Qian <i>et al.</i> [10]

#### Algorithm 1 Arbitrary Adverse Condition Generation With AdverseGAN

**Input:**  $C$ : input clean image;  $t$ : type label initialized to "00000";  $Codes$ : five binary codes from "00001" to "11111". Each digit represents a weather type, and from left to right, it represents haze, rain streak, snow, night, and raindrop in turn. '1' indicates that the condition contains that type of weather, while '0' is the opposite.

**Output:**  $D$ : degraded image

- 1: **for**  $i = 0$  to 4 **do**
- 2:     **if**  $Codes[i] = "1"$  **then**
- 3:          $t[i] = "1"$
- 4:         Sample  $z_c$  from  $\mathcal{N}(0, 1)$
- 5:         Sample  $z_s$  from  $\mathcal{N}(0, 1)$
- 6:          $C = AdverseGAN(C, t, z_c, z_s)$
- 7:          $t = "00000"$
- 8:  $D = C$
- 9: **return**  $D$

we generate 31 adverse scenes, each scene was randomly sampled twice from the style space and content space, resulting in 310K paired data. We also provide the algorithm procedures in Algo. 1 to better illustrate the training data generation pipeline. Moreover, we demonstrate the amazing generative power of AdverseGAN in Fig. 7.

Inevitably, the generated fake images would introduce undesired artifacts, which seems to compromise the training

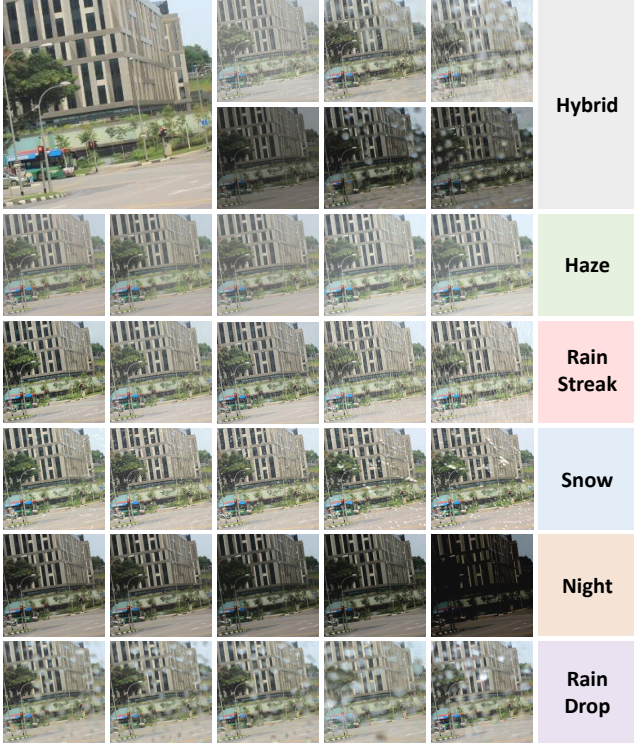


Fig. 7. Superimposed adverse conditions (top two rows) and interpolation results (bottom five rows) generated by AdverseGAN. AdverseGAN can generate infinite, controllable, realistic, and diverse adverse scenarios.

of the model, but we found the hazard of this to be minimal. As will be demonstrated in Sec. 4.3, RAHC trained only with data generated by AdverseGAN can achieve competitive results to the one trained on the standard training set and outperform most state-of-the-art methods.

### 3.4.2 Handcrafted Test Set

Since the training set can be generated by AdverseGAN, to guarantee the authority and accuracy of evaluation, the test set is carefully fabricated artificially. We first capture 200 high-quality well-curated images ( $720 \times 480$ ) as ground truth with Canon EOS 60D, and then synthesize corresponding 31 adverse conditions for each image, resulting in 6200 image pairs. The synthesis of haze, rain streak, snow, night, and raindrop follows previous academic literature [26], [34], [68], [72], [73]. Photoshop-related works were performed by three photography experts we recruited. Lighting conditions, scenes, subjects, and styles, e.g., are all taken into account to ensure realism and diversity.

To the best of our knowledge, HAC covers the wealthiest of adverse conditions and owns the largest amount of data. In some way, AdverseGAN can generate infinite adverse conditions. In Tab. 2, we compare HAC to other adverse conditions restoration datasets. These datasets only focus on single or double degradations, while our HAC dataset covers 31 scenarios combined by five types of weather.

## 4 EXPERIMENTS AND ANALYSIS

In this section, we conduct extensive experiments to demonstrate the effectiveness of the proposed method. We first

TABLE 2  
Comparison of HAC against conventional adverse conditions restoration datasets.

Dataset	Haze	Rain	Snow	Night	Raindrop	Total
RESIDE [68]	✓					~87K
Rain1200 [7]		✓				13.2K
Snow100K [34]			✓			100K
SICE [70]				✓		~0.6K
Raindrop [10]					✓	~1.1K
Outdoor-Rain [25]	✓	✓				10.5K
DarkRain [27]		✓		✓		~5K
RainDS [26]		✓			✓	5.8K
HAC	✓	✓	✓	✓	✓	~316K

present a detailed experimental setup in Section 4.1 and qualitative and quantitative comparisons with state-of-the-art methods are performed in Sections 4.2 and 4.3. The performance in real-world hybrid scenarios is verified in Section 4.4. We then performed ablation experiments on the restoration framework RAHC and the adverse weather generator AdverseGAN in Section 4.5 and Section 4.6, respectively. The complexity of the model is subsequently analyzed in Section 4.7. Finally, we further explored the application to high-level vision tasks in Section 4.8.

### 4.1 Implementation Details

All experiments are implemented with the Pytorch framework on two NVIDIA RTX 3090ti GPUs. For AdverseGAN, we use Adam as the optimizer with a batch size of 16, the learning rate is initialized to 0.00001 and then decreased to 0.000005 after 200 epochs. Once the network structure is determined, the size of the generated image is fixed, so the training data are randomly cropped to  $256 \times 256$ . We trained from scratch for 400 epochs on the above-mentioned datasets. Considering the differences in the number of different datasets, the resampling strategy is applied throughout the training process. For the restoration network, the number of MHBBs in different layers  $n_1 \sim n_8$  is set to 2, 4, 6, 4, 4, 2, 2, and 2, respectively. The number of heads is symmetrical, set to 1, 2, 4, and 8 in order from shallow to deep layers. We train our RAHC for  $6 \times 10^5$  iterations using Adam as the optimizer with a batch size of 4, except for the first 5K iterations where the mapping network is solely trained to avoid cold-start. The initial learning rate is  $2 \times 10^{-4}$ , which is steadily decreased to  $1 \times 10^{-6}$  using the cosine annealing strategy [74]. Notably, all methods in the comparison are trained on the same dataset until convergence with default configurations for a fair comparison. PSNR [75] and SSIM [76] are utilized to evaluate the restoration performance. These metrics are calculated in the RGB color space except for deraining on Rain1200 [7] where PSNR and SSIM are calculated on the Y channel in the YCbCr color space as in other works [15], [16]. The implementation code and dataset are available at <https://github.com/Jeasco/RAHC>.

### 4.2 Comparison with the State-of-the-Arts on HAC Dataset

The quantitative results on HAC dataset are reported in Tab. 3. As can be found, our RAHC delivers unparalleled

TABLE 3

Quantitative comparison with the SOTA methods on our proposed benchmark HAC dataset. Top super row: single model instance for single condition (condition-specific). Bottom super row: one model instance for all conditions (all-in-one). Multiplicative numeral indicates the number of weather types contained in an image (e.g., Triple represents the average scores of  $C_5^3 = 10$  conditions containing three weather types).

Method	Single		Double		Triple		Quadruple		Pentuple		Average	
	PSNR	SSIM	PSNR	SSIM	PSNR	SSIM	PSNR	SSIM	PSNR	SSIM	PSNR	SSIM
MIRNet [35]	28.44	0.9285	22.10	0.8749	19.11	0.7940	15.74	0.6483	14.30	0.6257	19.94	0.7743
HINet [36]	28.99	0.9393	23.33	0.9101	20.48	0.8422	16.14	0.6982	14.69	0.6689	20.73	0.8117
MPRNet [15]	28.84	0.9322	22.79	0.9147	20.19	0.8375	15.99	0.6858	14.65	0.6653	20.49	0.8071
SwinIR [18]	29.08	0.9411	24.21	0.9199	20.85	0.8517	16.78	0.7599	14.87	0.6672	21.16	0.8280
Uformer [19]	29.17	0.9425	24.48	0.9228	21.05	0.8533	16.89	0.7683	14.95	0.6728	21.31	0.8319
Restormer [16]	29.30	0.9478	24.60	0.9239	21.08	0.8531	16.92	0.7701	15.04	0.6783	21.39	0.8350
NAFNet [17]	29.35	0.9513	24.71	0.9276	21.12	0.8583	17.01	0.7864	15.23	0.6844	21.48	0.8416
RAHC	29.45	0.9517	24.98	0.9298	22.03	0.8817	19.53	0.8395	18.09	0.7502	22.82	0.8706
NAFNet [17]	29.10	0.9407	24.22	0.9143	20.74	0.8465	15.83	0.6623	14.33	0.6287	20.84	0.7985
TransWeather [23]	29.16	0.9433	24.25	0.9155	20.83	0.8495	16.72	0.7555	14.72	0.6652	21.14	0.8258
WeatherDiff [24]	29.19	0.9431	24.36	0.9215	20.99	0.8530	16.90	0.7685	14.93	0.6711	21.27	0.8314
AirNet [22]	29.19	0.9436	24.32	0.9207	20.97	0.8522	16.87	0.7655	15.01	0.6741	21.27	0.8312
TKL [20]	29.23	0.9441	24.36	0.9229	21.05	0.8531	16.93	0.7725	14.92	0.6734	21.30	0.8332
RAHC	29.40	0.9514	24.91	0.9283	22.17	0.8946	19.88	0.8425	18.24	0.7612	22.92	0.8756

performance gains and outperforms all competitive models both in the condition-specific setting and in the all-in-one setting, especially for extremely adverse scenarios such as “Quadruple” and “Pentuple”. Notably, RAHC exceeds the top-performing unified approach TKL [20] by 3.32dB on PSNR when there are pentuple degradation types. Furthermore, RAHC trained in the all-in-one setting even surpasses the results separately trained in each single condition. This phenomenon can be ascribed to the fact that the proposed discriminative learning scheme allows the network to learn more generalized and degradation-agnostic repair capabilities, and that the reconstruction vectors aided scheme can benefit from more sufficient data. We also demonstrate visual comparisons in Fig. 8 and Fig. 9. As suggested, RAHC recovers clean and crisp results while achieving a harmonious global tone without introducing visible artifacts or color shifts suffered by other methods, especially for complicated hybrid scenarios.

### 4.3 Comparison with the State-of-the-Arts on Conventional Datasets

In addition to HAC, we also evaluate the performance of RAHC on five conventional adverse weather removal datasets: Snow100K [34], Raindrop [10], SOTS-outdoor [68], Rain1200 [7], and SICE [70]. And only the training sets from these datasets are utilized to train AdverseGAN, so there is no information leakage. In addition, real-world images used for training AdverseGAN are replaced by handcrafted images in the corresponding datasets to better verify the data distribution simulation performance of AdverseGAN. The quantitative experimental results are presented in Tab. 4, Tab. 5, Tab. 6, Tab. 7, and Tab. 8 respectively.

In the tables, we provide the results of four types of experiments: (1) task-specific setting that is training with task-specific data only; (2) all-in-one setting that is training with mixed data from all datasets; (3) training with pure data generated by AdverseGAN; (4) the performance gain from applying AdverseGAN as a data augmentor.

As can be seen, our RAHC achieves the best scores on all five tasks both in the task-specific setting and in the

all-in-one setting. Take Tab. 7 for example, our method outperforms previous SOTA TKL [20] by a PSNR margin of up to 0.3dB. Moreover, with the all-in-one setting, our RAHC is only slightly inferior to the task-specific results, demonstrating consistent restoration performance.

To verify the reliability and distribution simulation capability of AdverseGAN, we trained RAHC only with data generated by AdverseGAN without original degraded images. As we have seen, RAHC trained from the generated data achieves competitive results, although tolerably worse than the standard results, this is negligible compared to the tedious and labor-intensive data synthesis process. And after all, both qualitative and quantitative experimental results on the HAC dataset demonstrate the plausibility of AdverseGAN. The results also indicate that our proposed AdverseGAN is trustworthy and excellent in simulating the source distribution, thus can perform as an augmentor to boost performance gains to existing methods.

Apart from the above experiments, we also provide the performance gain from applying AdverseGAN as an augmentor in parenthesis. Obviously, AdverseGAN delivers consistent performance gains for both task-specific and all-in-one approaches. Compared to task-specific approaches, the unified frameworks can obtain higher performance gains from augmentation, manifesting the importance of adequate training data for multi-weather learning.

### 4.4 Comparison with the State-of-the-Arts on Real-World Conditions

We conduct additional comparisons on real-world adverse weather conditions to further verify the realistic reliability of HAC and the robustness of RAHC. We use NIQE [84] and SSEQ [85] to quantitatively evaluate the reference-free restoration performance. Quantitative results are shown in Tab. 9. The smaller scores of SSEQ and NIQE indicate better perceptual quality and clearer contents. It is observed that our RAHC delivers the best average scores on real-world samples, outperforming the state-of-the-art restoration methods [20], [22], [23] by a large margin. Moreover,

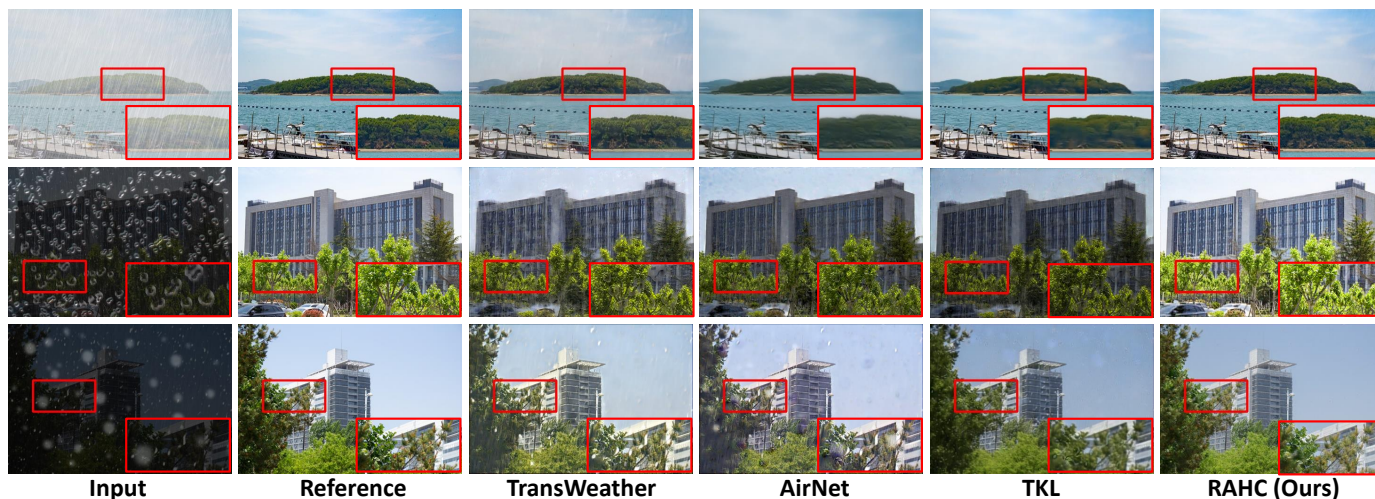


Fig. 8. Visual comparisons with SOTA adverse conditions restoration methods on outdoor natural scenery. Our RAHC restores more visually pleasing results with finer details and consistent illumination.

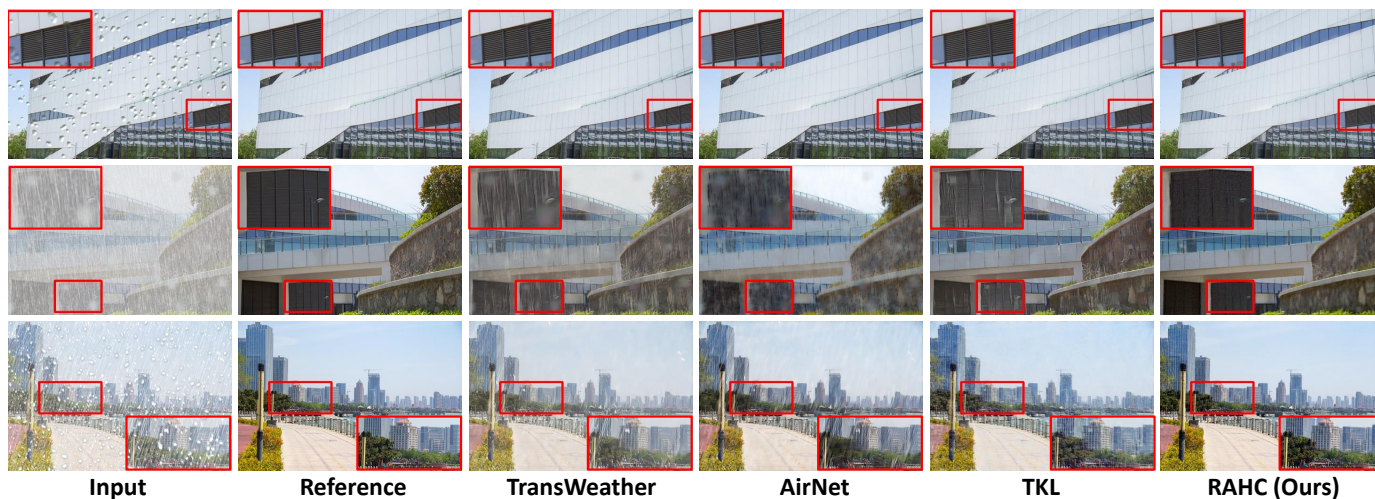


Fig. 9. Visual comparisons with SOTA adverse conditions restoration methods on outdoor building structures. Our RAHC restores more photorealistic results with coherent fine structural and textural details.

TABLE 4

Quantitative comparisons with the SOTA methods on the Snow100K [34] dataset. Top super row: training with task-specific data. Bottom super row: training with mixed data. † indicates training with pure data generated by AdverseGAN. The performance gain from applying AdverseGAN is reported in parenthesis.

Method	Snow100K-S		Snow100K-M		Snow100K-L	
	PSNR	SSIM	PSNR	SSIM	PSNR	SSIM
DesnowNet [34]	32.33	0.9500	30.87	0.9409	27.17	0.8983
DDMSNet [77]	34.34	0.9445	32.89	0.9330	28.85	0.8772
MPRNet [15]	35.25	0.9537	33.02	0.9422	30.30	0.8999
HDCWNet [9]	35.28 (0.07)	0.9571	33.14 (0.09)	0.9436	30.49 (0.14)	0.9017
NAFNet [17]	35.68 (0.06)	0.9609	33.80 (0.11)	0.9479	30.99 (0.17)	0.9084
RAHC	35.81 (0.09)	0.9647	34.03 (0.13)	0.9525	31.45 (0.16)	0.9189
RAHC†	35.32	0.9584	33.25	0.9421	30.56	0.9009
All-in-One [21]	-	-	-	-	28.33	0.8820
TransWeather [23]	35.21 (0.09)	0.9532	33.02 (0.16)	0.9408	30.28 (0.18)	0.8987
AirNet [22]	35.37 (0.09)	0.9584	33.24 (0.15)	0.9419	30.41 (0.19)	0.9087
TKL [20]	35.44 (0.08)	0.9597	33.38 (0.14)	0.9428	30.52 (0.17)	0.9098
RAHC	35.53 (0.11)	0.9625	33.66 (0.17)	0.9457	31.08 (0.23)	0.9115

TABLE 5

Quantitative comparison with the SOTA methods on the Raindrop removal test dataset [10]. Please refer to Tab. 4 for table notes.

Method	Raindrop	
	PSNR	SSIM
pix2pix [78]	28.02	0.8547
Quan [8]	31.44	0.9263
DuRN [79]	31.24 (0.18)	0.9259
Restormer [16]	32.69 (0.14)	0.9407
NAFNet [17]	32.51 (0.16)	0.9322
RAHC	33.37 (0.15)	0.9445
RAHC†	32.25	0.9326
All-in-One [21]	31.12	0.9268
TransWeather [23]	31.74 (0.22)	0.9279
AirNet [22]	32.27 (0.18)	0.9315
TKL [20]	32.35 (0.19)	0.9341
RAHC	32.82 (0.24)	0.9401

**TABLE 6**  
Quantitative comparison with the SOTA methods on the SOTS-outdoor [68] dataset. Please refer to Tab. 4 for table notes.

Method	SOTS-outdoor	
	PSNR	SSIM
GridDehazeNet [6]	31.47	0.9779
MPRNet [15]	32.17	0.9799
FFA-Net [31]	32.89	0.9802
AECR-Net [32]	33.07 (0.14)	0.9804
DehazeFormer [33]	33.22 (0.10)	0.9814
RAHC	33.89 (0.16)	0.9897
RAHC <sup>†</sup>	33.24	0.9809
TransWeather [23]	33.01 (0.20)	0.9768
AirNet [22]	33.09 (0.19)	0.9808
TKL [20]	33.13 (0.17)	0.9792
RAHC	33.54 (0.22)	0.9865

**TABLE 7**  
Quantitative comparison with the SOTA methods on the Rain1200 [7] dataset. Please refer to Tab. 4 for table notes.

Method	Rain1200	
	PSNR	SSIM
DDN [30]	30.97	0.9116
PReNet [80]	33.17	0.9481
RCDNet [12]	34.08	0.9532
Restormer [72]	34.67 (0.12)	0.9623
NAFNet [17]	34.69 (0.08)	0.9617
RAHC	34.93 (0.11)	0.9652
RAHC <sup>†</sup>	34.25	0.9572
TransWeather [23]	34.05 (0.16)	0.9535
AirNet [22]	34.19 (0.13)	0.9562
TKL [20]	34.25 (0.15)	0.9549
RAHC	34.71 (0.14)	0.9641

**TABLE 8**  
Quantitative comparison with the SOTA methods on the SICE [70] test dataset. Please refer to Tab. 4 for table notes.

Method	SICE	
	PSNR	SSIM
RUAS [13]	15.26	0.5481
EnlightenGAN [81]	17.55	0.5915
SCI [82]	19.26	0.6324
KinD [5]	20.13 (0.09)	0.6502
MIRNetv2 [83]	21.37 (0.15)	0.7203
RAHC	22.73 (0.14)	0.7425
RAHC <sup>†</sup>	21.09	0.6705
TransWeather [23]	20.42 (0.14)	0.6973
AirNet [22]	20.65 (0.18)	0.6993
TKL [20]	21.26 (0.16)	0.7131
RAHC	21.56 (0.18)	0.7269

**TABLE 9**  
Quantitative comparison results of average NIQE/SSEQ on real-world adverse weather conditions. The smaller scores indicate better perceptual quality.

Method	TransWeather [23]	AirNet [22]	TKL [20]	RAHC
NIQE	6.918	7.266	5.625	4.514
SSEQ	50.17	45.66	40.11	30.62

**TABLE 10**  
Average PSNR of RAHC on HAC dataset with four variants. RVA and OSD represent reconstruction vectors aided scheme and output space discriminative learning scheme respectively.

Variant	PSNR
RAHC w/o RVA	21.96
RAHC w/o OSD	22.41
RAHC w/o RVA&OSD	21.47
Ours	22.92

**TABLE 11**  
Average PSNR of RAHC on HAC dataset with five variants.

Variant	PSNR
MHBB w/o multi-head	22.59
CAM w/o convolution path	22.66
CAM w/o attention path	22.61
DP-FFN w/o convolution path	22.71
Ours	22.92



Fig. 10. Visual comparisons with SOTA adverse conditions restoration methods on real-world examples.

Fig. 10 exhibits the visual comparisons on real-world conditions. It can be seen that RAHC and TKL trained on HAC dataset can comfortably handle real-world hybrid adverse weather conditions, adequately indicating the realism and effectiveness of our proposed dataset. Meanwhile, our RAHC produces cleaner and more pleasing results compared to TKL and TransWeather, which strongly proves the superiority of our proposed RAHC. Additionally, this experiment also reveals the truth that real-world scenarios often suffer from multiple superimposed degradations rather than simple one corruption, and our method can flexibly restore arbitrary hybrid conditions in one go.

## 4.5 Analyzing Framework RAHC

### 4.5.1 Effect of Basic Schemes

We first investigate the validity of the reconstruction vectors aided scheme and the output space discriminative learning scheme proposed in this paper. Tab. 10 reports the ablations of the two basic schemes, and as we can see, the PSNR of RAHC w/o OSD decreases by 0.51dB, and a sharp reduction of 0.96dB was observed when RVA was discarded. The output space discriminative learning scheme ensures that the network learns degradation-agnostic generic repair capabilities while the reconstruction vectors aided scheme provides solid support for the network to cope with hybrid complicated adverse scenarios. The experimental results strongly demonstrate the indispensability of these two schemes, which have been instrumental in achieving arbitrary hybrid adverse weather conditions restoration.

### 4.5.2 Effect of MHBB

In order to verify the effectiveness of each pivotal design element in MHBB, we then conduct experiments over the following variants: (1) MHBB w/o multi-head; (2) CAM w/o convolution path; (3) CAM w/o attention path; (4) DP-FFN w/o convolution path; (5) Ours. It is necessary to note

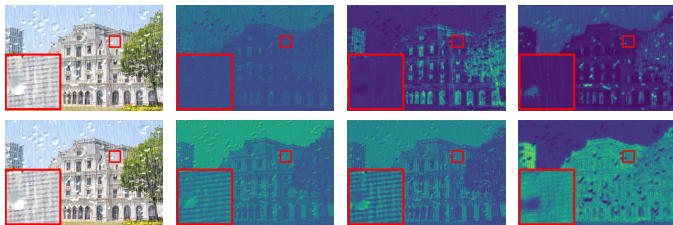


Fig. 11. Visual effect of DP-FFN with or without convolution path. Top row: feature maps extracted by the original FFN without convolutional path. Bottom row: feature maps extracted by the proposed DP-FFN with convolutional path.

that for each variant we adjust the width of the network to maintain the total number of parameters. As can be found in Tab. 11, each of the components plays a pivotal role, and removing any of them causes significant performance degradation. In particular, the PSNR decreases by 0.33dB when the multi-head mechanism is eliminated, indicating the profound effect of multiple representation subspace for degradation-agnostic learning.

Besides, we also provide a feature map comparison of DP-FFN with or without convolution path in Fig. 11. It is observed that the original FFN is insensitive to the local detail context and the extracted features ignore the building texture in the image, instead, our method extracts the rich building texture structure by parallelizing a convolutional branch afterward. The results clearly demonstrate that our proposed DP-FFN can better extract the detailed contexts of interest in image restoration by parallelizing a convolution path.

#### 4.5.3 Effect of Reconstruction Vectors

We also explored the effect of reconstruction vectors, and the visual results are provided in Fig. 12. As suggested, RAHC without RV tends to produce ambiguous contexts while our RAHC can restore sharper structural and textural details. Naturally, recovering clean images from the reconstruction vectors directly using the VQGAN decoder may be another option, but in this paper, we only leverage the reconstruction vectors as auxiliary features and let the network learn how to utilize them on its own. Such strategy can also be demonstrated by Fig. 12. We can see that the directly restored images (Visualization of RV) complement the possible textures of the degraded region but with low fidelity, while our implicit modeling allows the restoration model to use the visual atoms embedded in the reconstruction vector according to its own “experience”, hence restoring more realistic and reliable images with rich details.

Additionally, we also proffer the accuracy comparison of the proposed mapping network and direct classification in reconstruction vectors localization. As shown in Fig. 13, our method exhibits consistently higher accuracy than classification, not sensitive to high-precision predictions, the close-fitting reconstruction vectors can provide rich visual cues for the restoration process, as best demonstrated in Fig. 12.

#### 4.5.4 Objective Evaluation of Output Space Discriminative Learning Scheme

To verify whether the output space discriminative learning scheme yields degradation-agnostic and trace-free clean re-

TABLE 12

Average probability predicted by the weather type classifier. A lower confidence level indicates that the recovery results are perceptually closer to expected clean ones.

Method	Avg. Probability ( $\downarrow$ )
TransWeather [23]	0.553
AirNet [22]	0.528
TKL [20]	0.496
RAHC w/o OSD	0.452
RAHC (Ours)	0.231

TABLE 13

Comparison of feature-level discrimination and output space discrimination.

Variant	PSNR	SSIM
None	22.41	0.8652
Feature-Level	22.71	0.8735
Output Space (Ours)	22.92	0.8756

sults, we objectively evaluated the perceptual satisfaction of the restoration results. We first train a ResNet-101 [86] classifier with half of the data from the HAC test set to recognize which weather degradation is contained in the image. Then we input the rest data repaired by the restoration network to the trained classifier to get the predicted probability. Tab. 12 presents the average probability predicted by the weather type classifier. As we can see, our RAHC restores more indiscernible images, suggesting a more consistent and trace-free clean result. When this scheme is eliminated, the probability becomes significantly higher indicating the indelible role of the proposed learning scheme in the degradation-agnostic restoration. Despite OSD being removed, the probability is still lower than other approaches, which can be attributed to the proposed restoration network that allows the restored image to preserve more structural and textural details, thus closer to the desired clean result.

#### 4.5.5 Feature-Level Discrimination vs. Output Space Discrimination

Analogous to the output space discrimination, we further investigate feature-level discrimination that is input the encoder-extracted features into the discriminator to distinguish the type of degradation while the restoration network tries to confuse the discriminator to extract degradation-agnostic features. Quantitative experimental results are shown in Tab. 13, as can be found, both feature-level and output space contribute to learning degradation-agnostic restoration capacity while our output space is more favored compared to the counterpart. We conjecture that intermediate features containing high-level semantics are more prone to perplex the discriminator, which leads to weaker binding of the discriminator.

#### 4.5.6 Universal Output Space Discrimination

As mentioned above, our proposed output space discriminative learning scheme can be integrated into existing universal image restoration architectures boosting their performance under all-in-one setting. Similarly, TKL proposed by Chen *et al.* can also be applied to existing algorithms, and

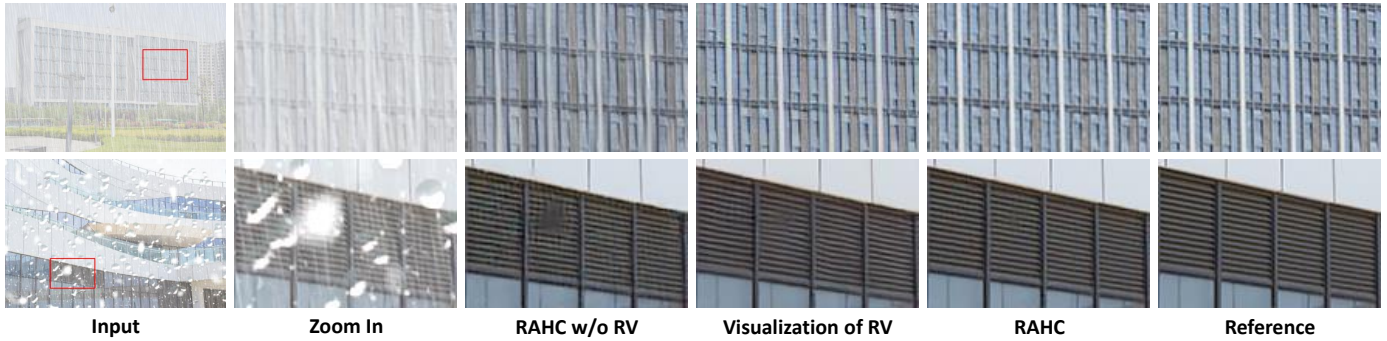


Fig. 12. Visual effect of reconstruction vectors. Visualizations of reconstruction vectors were obtained by the VQGAN decoder. RV represents reconstruction vectors.

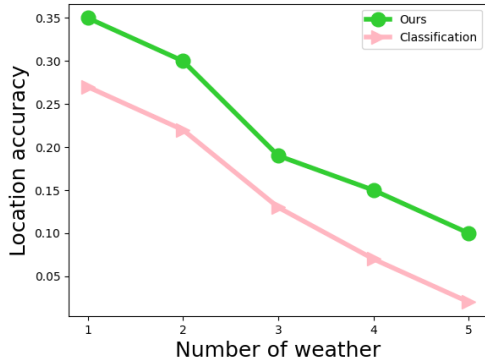


Fig. 13. Curve comparison on reconstruction vectors location accuracy.

TABLE 14

Results of applying TKL strategy proposed by Chen *et al.* [20] (top rows) and output space discriminative learning scheme proposed in this study (middle rows) into SOTA universal image restoration methods. Performance gains compared to pure training process are provided in parenthesis.

Method	PSNR	SSIM
MPRNet [15]	20.26 (↑ 0.58)	0.7812 (↑ 0.0383)
SwinIR [18]	21.01 (↑ 0.36)	0.8163 (↑ 0.0256)
Uformer [19]	21.03 (↑ 0.28)	0.8197 (↑ 0.0264)
Restormer [16]	21.14 (↑ 0.30)	0.8156 (↑ 0.0172)
NAFNet [17]	21.22 (↑ 0.38)	0.8215 (↑ 0.0230)
MPRNet [15]	20.33 (↑ 0.65)	0.7866 (↑ 0.0437)
SwinIR [18]	21.09 (↑ 0.44)	0.8213 (↑ 0.0306)
Uformer [19]	21.16 (↑ 0.41)	0.8217 (↑ 0.0284)
Restormer [16]	21.31 (↑ 0.47)	0.8301 (↑ 0.0317)
NAFNet [17]	21.37 (↑ 0.53)	0.8339 (↑ 0.0354)
TransWeather [23]	21.14	0.8258
AirNet [22]	21.27	0.8312
TKL [20]	21.30	0.8332
RAHC	22.92	0.8756

we have compared the superiority and inferiority of the two approaches under a fair backbone. As presented in Tab. 14, all algorithms show a significant performance improvement under the all-in-one setting when the learning scheme is equipped which is more obvious and noticeable than the TKL strategy. In particular, Restormer [16] and NAFNet [17] even surpass the extant state-of-the-art unified framework TKL [20] with the original backbone in their paper and our mechanism is more flexible and straightforward compared to the complex training process of TKL’s two-stage strategy.

TABLE 15

Comparison of similarity between reconstruction outputs of different degraded versions. S, D, T, Q, and P represent Single, Double, Triple, Quadruple, and Pentuple respectively (e.g.,  $D \leftrightarrow S$  denotes similarity calculation between the restoration results of the double-degraded versions and the single-degraded versions that correspond to the same clean image).

Participating Data	TransWeather		TKL		RAHC (ours)	
	PSNR	SSIM	PSNR	SSIM	PSNR	SSIM
$D \leftrightarrow S$	22.06	0.869	22.26	0.851	25.44	0.926
$T \leftrightarrow S$	18.53	0.799	19.02	0.811	22.36	0.901
$Q \leftrightarrow S$	15.16	0.675	15.36	0.698	19.91	0.852
$P \leftrightarrow S$	12.11	0.612	13.78	0.621	18.22	0.745

The experiments provide strong evidence of the generality, universality, and effectiveness of our proposed output space discriminative learning scheme.

#### 4.5.7 Robust Hybrid Adverse Weather Conditions Restoration

Since our proposed HAC dataset contains different degraded versions of the same clean image we can further verify the robustness of different restoration algorithms by comparing the similarity between the restoration results of different degraded images. Considering that existing methods are designed primarily for single degradation scenarios, we calculate the similarity between the restoration results of the hybrid weather degradation versions and the corresponding single degradation versions. Higher similarity indicates more robust hybrid adverse weather conditions restoration capability. It can be observed from Tab. 15 that our RAHC-restored hybrid degraded images are much more similar to the repaired single degraded images, delivering 3.34dB higher PSNR than TKL [20] on  $T \leftrightarrow S$ . Especially when there are more hybrid species (e.g.,  $P \leftrightarrow S$ ) for which our superiority is more obvious. This result strongly demonstrates the superiority of our method in restoring hybrid adverse weather conditions, in particular, benefiting from the reconstruction vectors aided scheme, which allows RAHC to extract the image content features from the auxiliary visual cues to produce more promising results in hybrid scenarios.

#### 4.5.8 Effect and Sensitivity Analysis of $\lambda_{dis}$

We also conducted a pilot study to substantiate the effect of  $\lambda_{dis}$  on the proposed output space discriminative learning scheme. Tab. 16 shows the final performances of different

TABLE 16  
Average PSNR of RAHC on HAC dataset with different  $\lambda_{dis}$ .

$\lambda_{dis}$	0.01	0.05	0.10	0.15	0.20
PSNR	22.69	22.86	22.92	22.83	22.81

TABLE 17  
Average PSNR of RAHC with different adverse weather conditions generators. DD and DS represent dual discriminator scheme and dual space injection scheme respectively.

Generator	PSNR
pix2pix [78]	18.33
pix2pixHD [87]	18.56
CycleGAN [42]	19.69
StarGAN [88]	20.75
StarGAN v2 [89]	20.82
Kim <i>et al.</i> [64]	20.91
AdverseGAN w/o DD&DS	20.86
AdverseGAN w/o DD	21.78
AdverseGAN w/o DS	21.89
AdverseGAN (Ours)	22.92

$\lambda_{dis}$  values. Obviously, the highest PSNR is yielded when  $\lambda_{dis}$  is set to 0.10, and both decreasing and increasing result in minor performance degradation. Furthermore, despite there are minor fluctuations, the final performances remain stable without collapse, implying the stability and facility of the proposed discriminative learning scheme.

## 4.6 Analyzing Data Generator AdverseGAN

### 4.6.1 Effect of AdverseGAN

To substantiate the effectiveness of AdverseGAN and the tailored schemes, we first conduct experiments with SOTA image translation algorithms as well as variants of AdverseGAN on adverse conditions generation. As can be found in Tab. 17, the model trained with data generated by AdverseGAN achieves the highest PSNR of 22.92 dB, 2.17 dB higher than StarGAN [88]. In addition, the dual discriminator scheme and dual space injection scheme are indelible credits to our design which are specifically adapted to the adverse conditions generation task presented in this paper. These two tailored schemes bring consistent performance improvements providing solid data support for the training of restoration networks.

Furthermore, we also provide a visual comparison in Fig. 14, from which it can be seen that removing the P-Discriminator leads to inconsistent background perturbations while removing the R-Discriminator results in unrealistic snow. On the contrary, can generate snow sceneries containing multiple scales of snow effects with different density distributions at different scales, which are visually similar to real snow scenes and significantly more realistic than hand-made conditions.

### 4.6.2 Disentanglement of Style and Content

Interpolation of style and content are shown in Fig. 15. As we can see, the  $s$  code tend to control the form and direction of the weather degradations while the  $c$  code are mainly responsible for the position and density of the weather degradations. The disentanglement of style and content

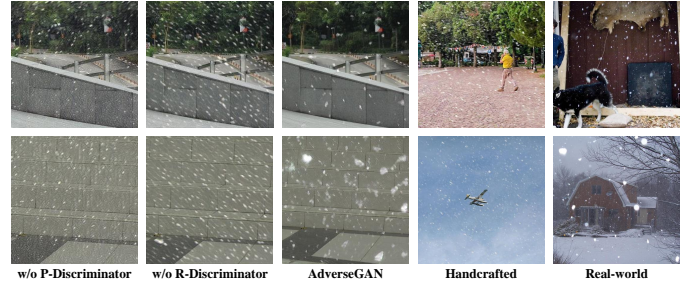


Fig. 14. Visual comparison of snow scenarios. Our AdverseGAN generates snow scenes that more closely resemble real-world condition and with consistent background.

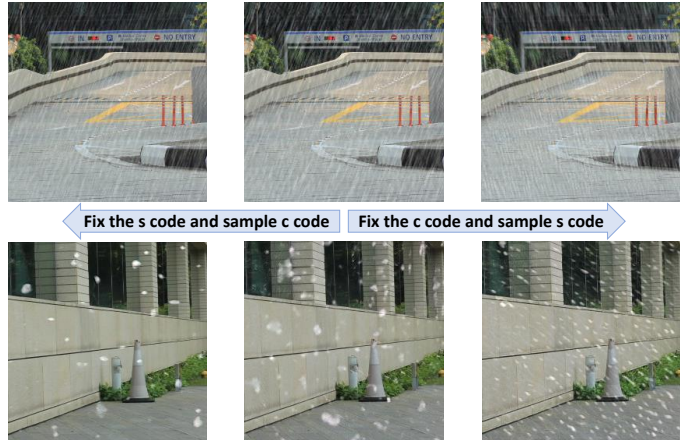


Fig. 15. Style interpolation and content interpolation.  $s$  code and  $c$  code are sampled from style space and content space respectively.

can better control the generation of adverse conditions and therefore produce richer and more diverse data.

### 4.6.3 The Amount of Training Data

We also substantiate the effect of different amounts of training data on the final performance of the model, and the experimental results are reported in Tab. 18. One can see that more training data can always lead to higher PSNR values, except that the frequency of growth continues to slow as the volume increases. In this paper, there are 310K training data in HAC, but as we can see from the trend, continuing to increase the training data will bring further performance improvements, only more computational resources are required.

## 4.7 Performance vs. Complexity

As it can be seen from Fig. 16, our RAHC obtains state-of-the-art performance at a moderate complexity and outperforms existing methods by a large margin. As a comparison, MIRNet [35], Restormer [16], and NAFNet [17] can only deal with single degradation scenarios, while AirNet [22] does require complicated additional regulation branch and

TABLE 18  
Average PSNR of RAHC on HAC dataset with different amount of training data.

Amount	31K	62K	124K	186K	248K	310K
PSNR	13.54	16.75	19.65	21.06	22.43	22.92

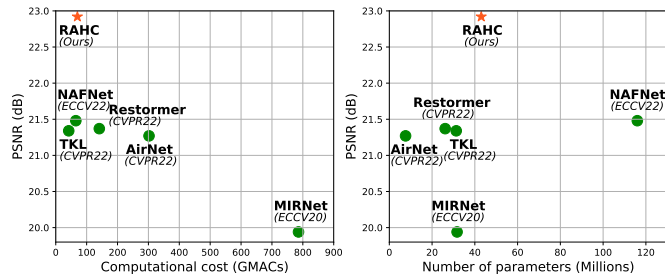


Fig. 16. Average PSNR vs. computational cost and parameter quantity on our proposed HAC dataset. The proposed RAHC obtains state-of-the-art performance with competitive computational cost and parameters.

TABLE 19

Quantitative results in mean intersection over union (mIoU) on ACDC [90] dataset with five adverse weather conditions (Both rain streaks and raindrops are included in Rain).

Method	Fog	Night	Rain	Snow
Original	43	11	37	29
Restormer [16]	46	27	39	31
TransWeather [23]	47	29	40	33
TKL [20]	49	27	41	34
RAHC (Ours)	54	36	45	36

TKL [20] suffers from two-stage training bringing unwanted resource consumption.

### 4.8 Results on High-level Application

To demonstrate the performance of the proposed restoration algorithm in real-world vision systems, we evaluate the effect of the restoration process on the popular adverse conditions segmentation dataset ACDC [90] with a pre-trained DeepLabv3+ [91]. As can be seen from Tab. 19, the unified framework TKL [20], TransWeather [23] and our RAHC achieve better results than single weather removal algorithm Restormer [16]. This phenomenon once again reveals the truth that real-world adverse weather conditions are sophisticated, unpredictable, and often the results of a mixture of weather factors. Single weather removal algorithm Restormer [16] can only remove specific weather at once, while unified frameworks can restore the complex scenario adaptively generating more appealing results. In addition, thanks to the application of reconstruction vectors and the output space constraint, our proposed RAHC attains significantly higher mIoU compared to TKL [20] and TransWeather [23]. This result also indicates the necessity and effectiveness of our proposed arbitrary hybrid adverse weather conditions restoration issue from the side. We also provide visual results of segmentation in Fig. 17. As we can see, our approach can better understand images in adverse conditions and more accurately identify the semantics of different regions.

## 5 DISCUSSION

Fig. 18 illustrates the restoration results of two real-world hybrid weather conditions. It can be easily noticed that processing each weather individually is unable to fully restore the degraded images, while our method can remove

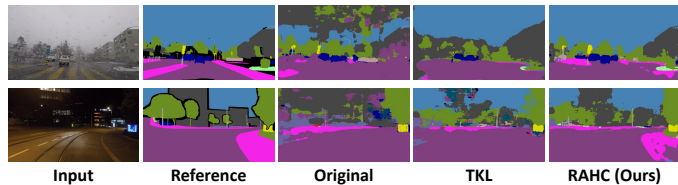


Fig. 17. Visual comparison of segmentation for driving scene understanding on ACDC [90] dataset between TKL [20] and our RAHC.

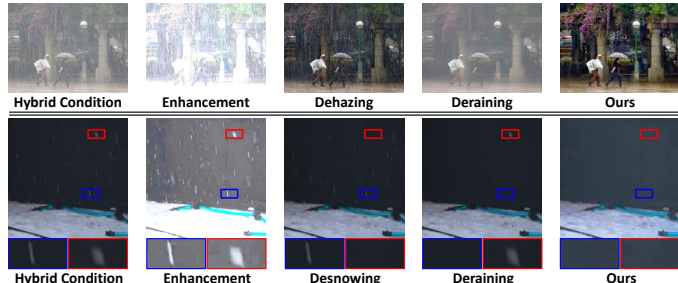


Fig. 18. Real-world hybrid adverse weather condition restoration results. Top row: an example with rain streaks, haze, and night. Bottom row: an example with rain streaks, snow, and night.

all degradations in one go to restore more pleasing high quality images. Besides, our RAHC can handle not only randomly occurring hybrid adverse weather conditions but also single weather scenarios robustly, thus our approach can be better deployed to tackle complex and diverse real-world conditions (without losing the ability to restore single weather degradations while can handle hybrid weather scenarios that are neglected by existing approaches). We believe the exploration in this study should be meaningful and valuable to real-world weather conditions restoration.

## 6 LIMITATIONS AND FUTURE WORK

A common limitation shared with other restoration algorithms is the strong reliance on large-scale paired data. As stated in the main paper, there are 310K pairs of data for model training. Fortunately, thanks to the proposed AdverseGAN, the labor cost, time cost, and capital cost is tremendously compressed. On the other hand, RAHC can handle arbitrary hybrid conditions combined by five common weather, while other rare adverse weather like frost on glass, sand and dust has remained to be addressed. In the future, we will focus on training models that can handle complicated hybrid conditions with single degraded data, which is extremely challenging but meaningful, especially when more weather types are taken into account, whose number of hybrid conditions grows exponentially. In addition, we will also explore more real-world nighttime adverse weather conditions simulation strategy in future research, which hopefully training more robust and practical image restoration models.

## 7 CONCLUDING REMARKS

In this paper, we proposed a novel unified framework, namely RAHC to restore arbitrary hybrid adverse weather conditions in one go. In contrast to existing frameworks, RAHC can handle severely deteriorated scenarios suffered from hybrid weather degradations and restore arbitrary

hybrid conditions with a single trained model by a concise and flexible scheme. Meanwhile, MHBB provides comprehensive degradation characterization and representation support for multiple simultaneous weather. In addition, we propose a hybrid adverse conditions generation pipeline, based on which sufficient training data can be generated cost-effectively. And then finally established HAC dataset contains  $\sim 316K$  image pairs of 31 weather conditions, which richness, diversity, and adequacy render it a competent evaluator. Extensive experiments on our HAC and conventional datasets manifest the effectiveness, superiority, and robustness of RACH. We expect this work to provide insights into arbitrary hybrid adverse conditions restoration and steer future research on this Gordian knot.

## REFERENCES

- [1] M. Liang, B. Yang, S. Wang, and R. Urtasun, "Deep continuous fusion for multi-sensor 3d object detection," in *Proceedings of the European conference on computer vision (ECCV)*, 2018, pp. 641–656.
- [2] A. Prakash, K. Chitta, and A. Geiger, "Multi-modal fusion transformer for end-to-end autonomous driving," in *Proceedings of the IEEE/CVF Conference on Computer Vision and Pattern Recognition*, 2021, pp. 7077–7087.
- [3] C. R. Qi, W. Liu, C. Wu, H. Su, and L. J. Guibas, "Frustum pointnets for 3d object detection from rgb-d data," in *Proceedings of the IEEE conference on computer vision and pattern recognition*, 2018, pp. 918–927.
- [4] A. G. Perera, Y. Wei Law, and J. Chahl, "Uav-gesture: A dataset for uav control and gesture recognition," in *Proceedings of the European Conference on Computer Vision (ECCV) Workshops*, 2018, pp. 0–0.
- [5] Y. Zhang, J. Zhang, and X. Guo, "Kindling the darkness: A practical low-light image enhancer," in *Proceedings of the 27th ACM international conference on multimedia*, 2019, pp. 1632–1640.
- [6] X. Liu, Y. Ma, Z. Shi, and J. Chen, "Griddehazenet: Attention-based multi-scale network for image dehazing," in *Proceedings of the IEEE/CVF international conference on computer vision*, 2019, pp. 7314–7323.
- [7] H. Zhang and V. M. Patel, "Density-aware single image de-raining using a multi-stream dense network," in *Proceedings of the IEEE conference on computer vision and pattern recognition*, 2018, pp. 695–704.
- [8] Y. Quan, S. Deng, Y. Chen, and H. Ji, "Deep learning for seeing through window with raindrops," in *Proceedings of the IEEE/CVF International Conference on Computer Vision*, 2019, pp. 2463–2471.
- [9] W.-T. Chen, H.-Y. Fang, C.-L. Hsieh, C.-C. Tsai, I. Chen, J.-J. Ding, S.-Y. Kuo *et al.*, "All snow removed: Single image desnowing algorithm using hierarchical dual-tree complex wavelet representation and contradict channel loss," in *Proceedings of the IEEE/CVF International Conference on Computer Vision*, 2021, pp. 4196–4205.
- [10] R. Qian, R. T. Tan, W. Yang, J. Su, and J. Liu, "Attentive generative adversarial network for raindrop removal from a single image," in *Proceedings of the IEEE conference on computer vision and pattern recognition*, 2018, pp. 2482–2491.
- [11] H. Dong, J. Pan, L. Xiang, Z. Hu, X. Zhang, F. Wang, and M.-H. Yang, "Multi-scale boosted dehazing network with dense feature fusion," in *Proceedings of the IEEE/CVF conference on computer vision and pattern recognition*, 2020, pp. 2157–2167.
- [12] H. Wang, Q. Xie, Q. Zhao, and D. Meng, "A model-driven deep neural network for single image rain removal," in *Proceedings of the IEEE/CVF Conference on Computer Vision and Pattern Recognition*, 2020, pp. 3103–3112.
- [13] R. Liu, L. Ma, J. Zhang, X. Fan, and Z. Luo, "Retinex-inspired unrolling with cooperative prior architecture search for low-light image enhancement," in *Proceedings of the IEEE/CVF Conference on Computer Vision and Pattern Recognition*, 2021, pp. 10 561–10 570.
- [14] M.-W. Shao, L. Li, D.-Y. Meng, and W.-M. Zuo, "Uncertainty guided multi-scale attention network for raindrop removal from a single image," *IEEE Transactions on Image Processing*, vol. 30, pp. 4828–4839, 2021.
- [15] S. W. Zamir, A. Arora, S. Khan, M. Hayat, F. S. Khan, M.-H. Yang, and L. Shao, "Multi-stage progressive image restoration," in *Proceedings of the IEEE/CVF conference on computer vision and pattern recognition*, 2021, pp. 14 821–14 831.
- [16] S. W. Zamir, A. Arora, S. Khan, M. Hayat, F. S. Khan, and M.-H. Yang, "Restormer: Efficient transformer for high-resolution image restoration," in *Proceedings of the IEEE/CVF Conference on Computer Vision and Pattern Recognition*, 2022, pp. 5728–5739.
- [17] L. Chen, X. Chu, X. Zhang, and J. Sun, "Simple baselines for image restoration," *arXiv preprint arXiv:2204.04676*, 2022.
- [18] J. Liang, J. Cao, G. Sun, K. Zhang, L. Van Gool, and R. Timofte, "Swinir: Image restoration using swin transformer," in *Proceedings of the IEEE/CVF International Conference on Computer Vision*, 2021, pp. 1833–1844.
- [19] Z. Wang, X. Cun, J. Bao, W. Zhou, J. Liu, and H. Li, "Uformer: A general u-shaped transformer for image restoration," in *Proceedings of the IEEE/CVF Conference on Computer Vision and Pattern Recognition*, 2022, pp. 17 683–17 693.
- [20] W.-T. Chen, Z.-K. Huang, C.-C. Tsai, H.-H. Yang, J.-J. Ding, and S.-Y. Kuo, "Learning multiple adverse weather removal via two-stage knowledge learning and multi-contrastive regularization: Toward a unified model," in *Proceedings of the IEEE/CVF Conference on Computer Vision and Pattern Recognition*, 2022, pp. 17 653–17 662.
- [21] R. Li, R. T. Tan, and L.-F. Cheong, "All in one bad weather removal using architectural search," in *Proceedings of the IEEE/CVF conference on computer vision and pattern recognition*, 2020, pp. 3175–3185.
- [22] B. Li, X. Liu, P. Hu, Z. Wu, J. Lv, and X. Peng, "All-In-One Image Restoration for Unknown Corruption," in *Proceedings of the IEEE/CVF Conference on Computer Vision and Pattern Recognition*, 2022, pp. 17 452–17 462.
- [23] J. M. J. Valanarasu, R. Yasarla, and V. M. Patel, "Transweather: Transformer-based restoration of images degraded by adverse weather conditions," in *Proceedings of the IEEE/CVF Conference on Computer Vision and Pattern Recognition*, 2022, pp. 2353–2363.
- [24] O. Özdenizci and R. Legenstein, "Restoring vision in adverse weather conditions with patch-based denoising diffusion models," *IEEE Transactions on Pattern Analysis and Machine Intelligence*, 2023.
- [25] R. Li, L.-F. Cheong, and R. T. Tan, "Heavy rain image restoration: Integrating physics model and conditional adversarial learning," in *Proceedings of the IEEE/CVF Conference on Computer Vision and Pattern Recognition*, 2019, pp. 1633–1642.
- [26] R. Quan, X. Yu, Y. Liang, and Y. Yang, "Removing raindrops and rain streaks in one go," in *Proceedings of the IEEE/CVF Conference on Computer Vision and Pattern Recognition*, 2021, pp. 9147–9156.
- [27] Y. Wan, Y. Cheng, M. Shao, and J. González, "Image rain removal and illumination enhancement done in one go," *Knowledge-Based Systems*, p. 109244, 2022.
- [28] A. Vaswani, N. Shazeer, N. Parmar, J. Uszkoreit, L. Jones, A. N. Gomez, L. Kaiser, and I. Polosukhin, "Attention is all you need," *Advances in neural information processing systems*, vol. 30, 2017.
- [29] P. Esser, R. Rombach, and B. Ommer, "Taming transformers for high-resolution image synthesis," in *Proceedings of the IEEE/CVF conference on computer vision and pattern recognition*, 2021, pp. 12 873–12 883.
- [30] X. Fu, J. Huang, D. Zeng, Y. Huang, X. Ding, and J. Paisley, "Removing rain from single images via a deep detail network," in *Proceedings of the IEEE conference on computer vision and pattern recognition*, 2017, pp. 3855–3863.
- [31] X. Qin, Z. Wang, Y. Bai, X. Xie, and H. Jia, "Ffa-net: Feature fusion attention network for single image dehazing," in *Proceedings of the AAAI Conference on Artificial Intelligence*, vol. 34, no. 07, 2020, pp. 11 908–11 915.
- [32] H. Wu, Y. Qu, S. Lin, J. Zhou, R. Qiao, Z. Zhang, Y. Xie, and L. Ma, "Contrastive learning for compact single image dehazing," in *Proceedings of the IEEE/CVF Conference on Computer Vision and Pattern Recognition*, 2021, pp. 10 551–10 560.
- [33] Y. Song, Z. He, H. Qian, and X. Du, "Vision transformers for single image dehazing," *arXiv preprint arXiv:2204.03883*, 2022.
- [34] Y.-F. Liu, D.-W. Jaw, S.-C. Huang, and J.-N. Hwang, "Desnownet: Context-aware deep network for snow removal," *IEEE Transactions on Image Processing*, vol. 27, no. 6, pp. 3064–3073, 2018.
- [35] S. W. Zamir, A. Arora, S. Khan, M. Hayat, F. S. Khan, M.-H. Yang, and L. Shao, "Learning enriched features for real image restoration and enhancement," in *European Conference on Computer Vision*. Springer, 2020, pp. 492–511.
- [36] L. Chen, X. Lu, J. Zhang, X. Chu, and C. Chen, "Hinet: Half instance normalization network for image restoration," in *Proceedings of the IEEE/CVF Conference on Computer Vision and Pattern Recognition*, 2021, pp. 182–192.

- [37] Y. Zhang, H. Ling, J. Gao, K. Yin, J.-F. Lafleche, A. Barriuso, A. Torralba, and S. Fidler, "Datasetgan: Efficient labeled data factory with minimal human effort," in *Proceedings of the IEEE/CVF Conference on Computer Vision and Pattern Recognition*, 2021, pp. 10 145–10 155.
- [38] Z. Yang, Y. Chai, D. Anguelov, Y. Zhou, P. Sun, D. Erhan, S. Raferty, and H. Kretschmar, "Surfelgan: Synthesizing realistic sensor data for autonomous driving," in *Proceedings of the IEEE/CVF Conference on Computer Vision and Pattern Recognition*, 2020, pp. 11 118–11 127.
- [39] H. Wang, Z. Yue, Q. Xie, Q. Zhao, Y. Zheng, and D. Meng, "From rain generation to rain removal," in *Proceedings of the IEEE/CVF Conference on Computer Vision and Pattern Recognition*, 2021, pp. 14 791–14 801.
- [40] Z. Liu, H. Yin, X. Wu, Z. Wu, Y. Mi, and S. Wang, "From shadow generation to shadow removal," in *Proceedings of the IEEE/CVF Conference on Computer Vision and Pattern Recognition*, 2021, pp. 4927–4936.
- [41] Z. Yue, Q. Zhao, L. Zhang, and D. Meng, "Dual adversarial network: Toward real-world noise removal and noise generation," in *European Conference on Computer Vision*. Springer, 2020, pp. 41–58.
- [42] J.-Y. Zhu, T. Park, P. Isola, and A. A. Efros, "Unpaired image-to-image translation using cycle-consistent adversarial networks," in *Proceedings of the IEEE international conference on computer vision*, 2017, pp. 2223–2232.
- [43] Y. Wei, Z. Zhang, Y. Wang, M. Xu, Y. Yang, S. Yan, and M. Wang, "Deraincyclegan: Rain attentive cyclegan for single image deraining and rainmaking," *IEEE Transactions on Image Processing*, vol. 30, pp. 4788–4801, 2021.
- [44] W. Yan, Y. Zhang, P. Abbeel, and A. Srinivas, "Videogpt: Video generation using vq-vae and transformers," *arXiv preprint arXiv:2104.10157*, 2021.
- [45] J. Yu, X. Li, J. Y. Koh, H. Zhang, R. Pang, J. Qin, A. Ku, Y. Xu, J. Baldridge, and Y. Wu, "Vector-quantized image modeling with improved vqgan," *arXiv preprint arXiv:2110.04627*, 2021.
- [46] A. Razavi, A. Van den Oord, and O. Vinyals, "Generating diverse high-fidelity images with vq-vae-2," *Advances in neural information processing systems*, vol. 32, 2019.
- [47] R. Rombach, A. Blattmann, D. Lorenz, P. Esser, and B. Ommer, "High-resolution image synthesis with latent diffusion models," in *Proceedings of the IEEE/CVF Conference on Computer Vision and Pattern Recognition*, 2022, pp. 10 684–10 695.
- [48] J. Hoffman, E. Tzeng, T. Park, J.-Y. Zhu, P. Isola, K. Saenko, A. Efros, and T. Darrell, "Cycada: Cycle-consistent adversarial domain adaptation," in *International conference on machine learning*. Pmlr, 2018, pp. 1989–1998.
- [49] G. Kang, Y. Wei, Y. Yang, Y. Zhuang, and A. Hauptmann, "Pixel-level cycle association: A new perspective for domain adaptive semantic segmentation," *Advances in Neural Information Processing Systems*, vol. 33, pp. 3569–3580, 2020.
- [50] Z. Murez, S. Kolouri, D. Kriegman, R. Ramamoorthi, and K. Kim, "Image to image translation for domain adaptation," in *Proceedings of the IEEE Conference on Computer Vision and Pattern Recognition*, 2018, pp. 4500–4509.
- [51] Y.-H. Tsai, W.-C. Hung, S. Schuster, K. Sohn, M.-H. Yang, and M. Chandraker, "Learning to adapt structured output space for semantic segmentation," in *Proceedings of the IEEE conference on computer vision and pattern recognition*, 2018, pp. 7472–7481.
- [52] Y. Luo, P. Liu, L. Zheng, T. Guan, J. Yu, and Y. Yang, "Category-level adversarial adaptation for semantic segmentation using purified features," *IEEE Transactions on Pattern Analysis and Machine Intelligence*, 2021.
- [53] Y. Luo, L. Zheng, T. Guan, J. Yu, and Y. Yang, "Taking a closer look at domain shift: Category-level adversaries for semantics consistent domain adaptation," in *Proceedings of the IEEE/CVF Conference on Computer Vision and Pattern Recognition*, 2019, pp. 2507–2516.
- [54] Y. Zou, Z. Yu, B. Kumar, and J. Wang, "Unsupervised domain adaptation for semantic segmentation via class-balanced self-training," in *Proceedings of the European conference on computer vision (ECCV)*, 2018, pp. 289–305.
- [55] K. Zhang, Y. Li, J. Liang, J. Cao, Y. Zhang, H. Tang, R. Timofte, and L. Van Gool, "Practical blind denoising via swin-conv-unet and data synthesis," *arXiv preprint arXiv:2203.13278*, 2022.
- [56] A. Gulati, J. Qin, C.-C. Chiu, N. Parmar, Y. Zhang, J. Yu, W. Han, S. Wang, Z. Zhang, Y. Wu *et al.*, "Conformer: Convolution-augmented transformer for speech recognition," *arXiv preprint arXiv:2005.08100*, 2020.
- [57] W. Shi, J. Caballero, F. Huszár, J. Totz, A. P. Aitken, R. Bishop, D. Rueckert, and Z. Wang, "Real-time single image and video super-resolution using an efficient sub-pixel convolutional neural network," in *Proceedings of the IEEE conference on computer vision and pattern recognition*, 2016, pp. 1874–1883.
- [58] A. Kuznetsova, H. Rom, N. Alldrin, J. Uijlings, I. Krasin, J. Pont-Tuset, S. Kamali, S. Popov, M. Mallocci, A. Kolesnikov *et al.*, "The open images dataset v4," *International Journal of Computer Vision*, vol. 128, no. 7, pp. 1956–1981, 2020.
- [59] J. Johnson, A. Alahi, and L. Fei-Fei, "Perceptual losses for real-time style transfer and super-resolution," in *European conference on computer vision*. Springer, 2016, pp. 694–711.
- [60] X. Pan, A. Tewari, L. Liu, and C. Theobalt, "Gan2x: Non-lambertian inverse rendering of image gans," *arXiv preprint arXiv:2206.09244*, 2022.
- [61] Y. Xu, Y. Yin, L. Jiang, Q. Wu, C. Zheng, C. C. Loy, B. Dai, and W. Wu, "Transeditor: Transformer-based dual-space gan for highly controllable facial editing," in *Proceedings of the IEEE/CVF Conference on Computer Vision and Pattern Recognition*, 2022, pp. 7683–7692.
- [62] G. Kwon and J. C. Ye, "Diagonal attention and style-based gan for content-style disentanglement in image generation and translation," in *Proceedings of the IEEE/CVF International Conference on Computer Vision*, 2021, pp. 13 980–13 989.
- [63] Y. Alharbi and P. Wonka, "Disentangled image generation through structured noise injection," in *Proceedings of the IEEE/CVF Conference on Computer Vision and Pattern Recognition*, 2020, pp. 5134–5142.
- [64] K. Kim, S. Park, E. Jeon, T. Kim, and D. Kim, "A style-aware discriminator for controllable image translation," in *Proceedings of the IEEE/CVF Conference on Computer Vision and Pattern Recognition*, 2022, pp. 18 239–18 248.
- [65] A. Van den Oord, N. Kalchbrenner, L. Espeholt, O. Vinyals, A. Graves *et al.*, "Conditional image generation with pixelcnn decoders," *Advances in neural information processing systems*, vol. 29, 2016.
- [66] T. Karras, S. Laine, M. Aittala, J. Hellsten, J. Lehtinen, and T. Aila, "Analyzing and improving the image quality of stylegan," in *Proceedings of the IEEE/CVF conference on computer vision and pattern recognition*, 2020, pp. 8110–8119.
- [67] A. Odena, C. Olah, and J. Shlens, "Conditional image synthesis with auxiliary classifier gans," in *International conference on machine learning*. PMLR, 2017, pp. 2642–2651.
- [68] B. Li, W. Ren, D. Fu, D. Tao, D. Feng, W. Zeng, and Z. Wang, "Benchmarking single-image dehazing and beyond," *IEEE Transactions on Image Processing*, vol. 28, no. 1, pp. 492–505, 2018.
- [69] W. Wei, D. Meng, Q. Zhao, Z. Xu, and Y. Wu, "Semi-supervised transfer learning for image rain removal," in *Proceedings of the IEEE/CVF conference on computer vision and pattern recognition*, 2019, pp. 3877–3886.
- [70] J. Cai, S. Gu, and L. Zhang, "Learning a deep single image contrast enhancer from multi-exposure images," *IEEE Transactions on Image Processing*, vol. 27, no. 4, pp. 2049–2062, 2018.
- [71] Y. P. Loh and C. S. Chan, "Getting to know low-light images with the exclusively dark dataset," *Computer Vision and Image Understanding*, vol. 178, pp. 30–42, 2019.
- [72] X. Fu, J. Huang, X. Ding, Y. Liao, and J. Paisley, "Clearing the skies: A deep network architecture for single-image rain removal," *IEEE Transactions on Image Processing*, vol. 26, no. 6, pp. 2944–2956, 2017.
- [73] C. Wei, W. Wang, W. Yang, and J. Liu, "Deep retinex decomposition for low-light enhancement," *arXiv preprint arXiv:1808.04560*, 2018.
- [74] I. Loshchilov and F. Hutter, "Sgdr: Stochastic gradient descent with warm restarts," *arXiv preprint arXiv:1608.03983*, 2016.
- [75] Q. Huynh-Thu and M. Ghanbari, "Scope of validity of psnr in image/video quality assessment," *Electronics letters*, vol. 44, no. 13, pp. 800–801, 2008.
- [76] Z. Wang, A. C. Bovik, H. R. Sheikh, and E. P. Simoncelli, "Image quality assessment: from error visibility to structural similarity," *IEEE transactions on image processing*, vol. 13, no. 4, pp. 600–612, 2004.
- [77] K. Zhang, R. Li, Y. Yu, W. Luo, and C. Li, "Deep dense multi-scale network for snow removal using semantic and depth priors," *IEEE Transactions on Image Processing*, vol. 30, pp. 7419–7431, 2021.

- [78] P. Isola, J.-Y. Zhu, T. Zhou, and A. A. Efros, "Image-to-image translation with conditional adversarial networks," in *Proceedings of the IEEE conference on computer vision and pattern recognition*, 2017, pp. 1125–1134.
- [79] X. Liu, M. Suganuma, Z. Sun, and T. Okatani, "Dual residual networks leveraging the potential of paired operations for image restoration," in *Proceedings of the IEEE/CVF Conference on Computer Vision and Pattern Recognition*, 2019, pp. 7007–7016.
- [80] D. Ren, W. Zuo, Q. Hu, P. Zhu, and D. Meng, "Progressive image deraining networks: A better and simpler baseline," in *Proceedings of the IEEE/CVF Conference on Computer Vision and Pattern Recognition*, 2019, pp. 3937–3946.
- [81] Y. Jiang, X. Gong, D. Liu, Y. Cheng, C. Fang, X. Shen, J. Yang, P. Zhou, and Z. Wang, "Enlightengan: Deep light enhancement without paired supervision," *IEEE Transactions on Image Processing*, vol. 30, pp. 2340–2349, 2021.
- [82] L. Ma, T. Ma, R. Liu, X. Fan, and Z. Luo, "Toward fast, flexible, and robust low-light image enhancement," in *Proceedings of the IEEE/CVF Conference on Computer Vision and Pattern Recognition*, 2022, pp. 5637–5646.
- [83] S. W. Zamir, A. Arora, S. Khan, M. Hayat, F. S. Khan, M.-H. Yang, and L. Shao, "Learning enriched features for fast image restoration and enhancement," *arXiv preprint arXiv:2205.01649*, 2022.
- [84] A. Mittal, R. Soundararajan, and A. C. Bovik, "Making a "completely blind" image quality analyzer," *IEEE Signal processing letters*, vol. 20, no. 3, pp. 209–212, 2012.
- [85] L. Liu, B. Liu, H. Huang, and A. C. Bovik, "No-reference image quality assessment based on spatial and spectral entropies," *Signal processing: Image communication*, vol. 29, no. 8, pp. 856–863, 2014.
- [86] K. He, X. Zhang, S. Ren, and J. Sun, "Deep residual learning for image recognition," in *Proceedings of the IEEE conference on computer vision and pattern recognition*, 2016, pp. 770–778.
- [87] T.-C. Wang, M.-Y. Liu, J.-Y. Zhu, A. Tao, J. Kautz, and B. Catanzaro, "High-resolution image synthesis and semantic manipulation with conditional gans," in *Proceedings of the IEEE conference on computer vision and pattern recognition*, 2018, pp. 8798–8807.
- [88] Y. Choi, M. Choi, M. Kim, J.-W. Ha, S. Kim, and J. Choo, "Stargan: Unified generative adversarial networks for multi-domain image-to-image translation," in *Proceedings of the IEEE conference on computer vision and pattern recognition*, 2018, pp. 8789–8797.
- [89] Y. Choi, Y. Uh, J. Yoo, and J.-W. Ha, "Stargan v2: Diverse image synthesis for multiple domains," in *Proceedings of the IEEE/CVF conference on computer vision and pattern recognition*, 2020, pp. 8188–8197.
- [90] C. Sakaridis, D. Dai, and L. Van Gool, "Acdc: The adverse conditions dataset with correspondences for semantic driving scene understanding," in *Proceedings of the IEEE/CVF International Conference on Computer Vision*, 2021, pp. 10765–10775.
- [91] L.-C. Chen, Y. Zhu, G. Papandreou, F. Schroff, and H. Adam, "Encoder-decoder with atrous separable convolution for semantic image segmentation," in *Proceedings of the European conference on computer vision (ECCV)*, 2018, pp. 801–818.



**Mingwen Shao** received his M.S. degree in mathematics from the Guangxi University, Guangxi, China, in 2002, and the Ph.D. degree in applied mathematics from Xi'an Jiaotong University, Xi'an, China, in 2005. He received the postdoctoral degree in control science and engineering from Tsinghua University in February 2008. Now he is a professor and doctoral supervisor at China University of Petroleum (East China). His research interests include machine learning, computer vision, and data mining.



**Yuanshuo Cheng** is a B.Eng. at College of Computer Science and Technology, China University of Petroleum (East China), under the supervision of Prof. Shao. His current research interests include image restoration, computer vision, and deep learning.



**Yuexian Liu** is a B.Eng. at College of Computer Science and Technology, China University of Petroleum (East China), under the supervision of Prof. Shao. His current research interests include image restoration and computer vision.



**Zhiyuan Bao** is a master student at College of Computer Science and Technology, China University of Petroleum (East China), under the supervision of Prof. Shao. He received the bachelor of software engineering from the China University of Petroleum (East China). His research interests include image restoration and computer vision.



**Deyu Meng** received the B.Sc., M.Sc., and Ph.D. degrees from Xi'an Jiaotong University, Xi'an, China, in 2001, 2004, and 2008, respectively. He was a Visiting Scholar with Carnegie Mellon University, Pittsburgh, PA, USA, from 2012 to 2014. He is currently a Professor with the Institute for Information and System Sciences, Xi'an Jiaotong University. His current research interests include self-paced learning, noise modeling, and tensor sparsity.



**Yecong Wan** is a B.Eng. at College of Computer Science and Technology, China University of Petroleum (East China), under the supervision of Prof. Shao. His current research interests include image restoration and computer vision.